Rapid-Scan and Polarimetric Radar Observations of the Dissipation of a Violent Tornado on 9 May 2016 near Sulphur, Oklahoma

KATHERINE E. MCKEOWN,[a] MICHAEL M. FRENCH, AND KRISTOFER S. TUFTEDAL

School of Marine and Atmospheric Sciences, Stony Brook University, State University of New York, Stony Brook, New York

DARREL M. KINGFIELD

Cooperative Institute for Research in Environmental Sciences, University of Colorado, and NOAA/OAR/ESRL/Global Systems Laboratory, Boulder, Colorado

HOWARD B. BLUESTEIN, DYLAN W. REIF, AND ZACHARY B. WIENHOFF[b]

School of Meteorology, University of Oklahoma, Norman, Oklahoma

(Manuscript received 31 January 2020, in final form 9 July 2020)

ABSTRACT

Rapid-scan polarimetric data analysis of the dissipation of a likely violent supercell tornado that struck near Sulphur, Oklahoma, on 9 May 2016 is presented. The Rapid X-band Polarimetric Radar was used to obtain data of the tornado at the end of its mature phase and during its entire dissipation phase. The analysis is presented in two parts: dissipation characteristics of the tornadic vortex signature (TVS) associated with the tornado and storm-scale polarimetric features that may be related to processes contributing to tornado dissipation. The TVS exhibited near-surface radial velocities exceeding 100 m s^{-1} multiple times at the end of its mature phase, and then underwent a two-phased dissipation. Initially, decreases in near-surface intensity occurred rapidly over a ~5-min period followed by a slower decline in intensity that lasted an additional ~12 min. The dissipation of the TVS in time and height in the lowest 2 km above radar level and oscillatory storm-relative motion of the TVS also are discussed. Using polarimetric data, a well-defined low reflectivity ribbon is investigated for its vertical development, evolution, and relationship to the large tornadic debris signature (TDS) collocated with the TVS. The progression of the TDS during dissipation also is discussed with a focus on the presence of several bands of reduced copolar correlation coefficient that extend away from the main TDS and the eventual erosion of the TDS as the tornado dissipated. Finally, TVS and polarimetric data are combined to argue for the importance of a possible internal rear-flank downdraft momentum surge in contributing to the initial rapid dissipation of the tornado.

1. Introduction

Mobile, ground-based Doppler radars have been used since the mid-1990s to investigate supercells and tornadoes with finer spatial resolution than that available using data from the stationary, operational Weather Surveillance Radar-1988 Doppler (WSR-88D) network (e.g., Bluestein et al. 1995; Wurman et al. 1997). A close range to the phenomenon of interest afforded by the mobility of the trucks and/or fine radar beamwidth on high-frequency systems ranging from 3-mm wavelength (W band) to 5-cm wavelength (C band) have allowed for previously unobserved small-scale features within supercells to be identified (e.g., Wurman and Gill 2000; Bluestein and Pazmany 2000; Wurman 2002).

A more recent focus of research is on leveraging mobile Doppler radars for their improved temporal volumetric sampling compared to operational radar networks. The volumetric update times of traditional mobile Doppler radars (i.e., non-rapid-scanning systems) are typically ~2 min up to storm midlevels versus ~300 s for full WSR-88D volumes, owing to shorter dwell times and dynamic sector scanning capabilities in

[a] Current affiliation: Department of Earth Sciences and Geography, University of North Carolina at Charlotte, Charlotte, North Carolina.
[b] Current affiliation: Wind Engineering Research Laboratory, University of Illinois at Urbana–Champaign, Urbana, Illinois.

Corresponding author: Michael M. French, michael.m.french@stonybrook.edu

DOI: 10.1175/MWR-D-20-0033.1

© 2020 American Meteorological Society. For information regarding reuse of this content and general copyright information, consult the AMS Copyright Policy (www.ametsoc.org/PUBSReuseLicenses).

Brought to you by NOAA Central Library | Unauthenticated | Downloaded 09/15/21 06:16 PM UTC

the former. Therefore, the data can be used to learn more about, for example, the evolution of the tornado life cycle (e.g., Bluestein et al. 2003; Alexander and Wurman 2005; Calhoun et al. 2013) or to investigate storm-scale processes like cyclic mesocyclogenesis (e.g., Beck et al. 2006; French et al. 2008) and hook echo formation and evolution (Byko et al. 2009). However, given that the advective time scale of a tornado is ~10 s (Bluestein et al. 2010), even finer temporal scales are needed to study volumetric tornado-scale processes. Newer systems like the Mobile Weather Radar, 2005 X-Band, Phased Array (MWR-05XP; Bluestein et al. 2010), the Rapid X-band Polarimetric Radar (RaXPol; Pazmany et al. 2013), and the Atmospheric Imaging Radar (AIR; Isom et al. 2013) all possess volumetric update times of ~5–20 s, making them ideal instruments to study tornado-scale processes. A main focus of studies using these systems has been on the short time scale and time–height evolution of tornadogenesis (French et al. 2013; Houser et al. 2015; Bluestein et al. 2019), tornado intensification (French et al. 2014; Bluestein et al. 2019) and tornado structure (e.g., French et al. 2015b; Wakimoto et al. 2016; Kurdzo et al. 2017; Bluestein et al. 2018; Mahre et al. 2018).

Despite the increasing number of rapid-scan datasets of supercell tornado life cycles, only a few studies have specifically examined the tornado *dissipation* process and the storm-scale evolution leading up to tornado dissipation. Tornado dissipation in supercells may not proceed similarly from case to case. Within the cyclic tornadogenesis process (Darkow and Roos 1970; Burgess et al. 1982), it is thought that storm-relative (SR) advection of the tornado away from areas of vertical vorticity production are likely to inhibit tornado maintenance (Dowell and Bluestein 2002b). Marquis et al. (2012) used Doppler on Wheels (DOW; Wurman et al. 1997) data to synthesize dual-Doppler and EnKF data assimilation analyses in several cases in an effort to study how tornado maintenance may be disrupted outside of the cycling process. They found several potential contributors to tornado demise including changes in the intensity of the rear-flank downdraft (RFD) outflow, separation of the tornado from the main storm updraft, lack of low-level convergence, and excessive outflow from secondary RFD gust front surges (hereinafter internal RFD momentum surges). In a subsequent case study of the Goshen County tornado, Marquis et al. (2016) also found that storm low-level and midlevel circulations were disconnected entering the dissipation phase of the tornado.

More recently, French and Kingfield (2019; hereinafter FK19) used past case study data to identify tornadic vortex signature (TVS) behaviors associated with dissipation in supercells. In 36 WSR-88D cases, they found that three of the behaviors, TVS intensity weakening, SR rearward motion, and large horizontal displacement from the main storm updraft, were consistently associated with dissipation. However, owing to the poor volumetric sampling of the WSR-88D systems, they could only identify these behaviors periodically over 20-min-long periods. Therefore, it is not known how the TVS dissipation behaviors evolve over very short time scales.

Studies of tornado dissipation that did use rapid-scan mobile Doppler radars have focused on the unique time–height evolution of the process. French et al. (2014) found that (i) three tornadoes dissipated first in the ~1–2-km level and last in the lowest 1 km and (ii) the TVSs moved in different directions below and above the level dissipation began at (increasing tilt). Subsequently, Houser et al. (2015) found dissipation evolution varied depending on how a TVS was defined, but observed rapid weakening at all levels and ΔV reductions below 40 m s^{-1} first in the same 1–2-km layer in one case. Griffin et al. (2019) observed in another case that dissipation occurred rapidly (~2 min) and first in the 1–2-km layer where tilt was maximized, then below 1 km. Despite the consistencies cited in these studies, only five dissipation cases analyzed belies a generalization of the time–height progression of tornado dissipation.

Finally, coincident with the advancement of rapid-scan radars has been the proliferation of dual-polarization mobile Doppler radars. Much of the tornadic supercell case study work using these systems has focused on the identification, structure, and evolution of tornadic debris signatures (TDSs; Ryzhkov et al. 2005) associated with tornadoes (e.g., Bluestein et al. 2007; Kurdzo et al. 2015; Wakimoto et al. 2015, 2018, 2020; Houser et al. 2016; Griffin et al. 2020). Only a subset of the aforementioned studies combined both rapid-scan *and* dual-polarization capabilities in observational analysis, owing to the difficulty in simultaneously achieving electronic scanning and unbiased dual linear polarization variable retrieval (e.g., Zrnić et al. 2011). Even fewer studies have used mobile polarimetric Doppler radar to examine the tornado dissipation process, particularly the evolution of storm-scale polarimetric features during dissipation. Only Houser et al. (2015) analyzed rapid-scan polarimetric radar data during tornado dissipation, but the focus was not on the evolution of polarimetric features during the dissipation process.

However, there is some indication that analysis of high-resolution polarimetric storm-scale supercell

Brought to you by NOAA Central Library | Unauthenticated | Downloaded 09/15/21 06:16 PM UTC

features may also allow for insight into the tornado life cycle, including tornado dissipation. Studies have noted some changes in the TDS during tornado dissipation or weakening, including more debris fallout (Bodine et al. 2013) and increasingly wide (narrow) TDSs at the surface (aloft) (Houser et al. 2016), both likely caused by weaker vertical velocities in the tornado. French et al. (2015a) used polarimetric radar data (mostly differential radar reflectivity factor Z_{DR}) to estimate bulk drop size distribution (DSD) properties in several supercells and found increasing hook echo median raindrop sizes leading up to and during tornado dissipation in three cases using data from a mobile, X-band Doppler radar. They speculated that a higher median drop size may indicate a greater evaporation rate and an influx of negatively buoyant air at the surface in the RFD region that disrupts tornado maintenance. However, there have not been any additional cases investigated to determine if the observed increase in bulk drop size is a common feature in supercells when tornadoes dissipate.

Ultimately, few studies have ventured to use mobile Doppler, rapid-scan, polarimetric radar data to understand the physical characteristics of dissipating tornadoes and the storm-scale features associated with the dissipation process, partially due to lack of sufficient finescale observations. Because the WSR-88D network only has volumetric updates every ~5 min, this line of research must rely on case studies and the availability of high-spatiotemporal-resolution data of the process. In this paper, we detail tornado- and storm-scale radar observations obtained by RaXPol of the dissipation of a strong, and likely violent, tornado that struck near Sulphur, Oklahoma, on 9 May 2016. RaXPol observations are supplemented by KTLX WSR-88D observations of the same tornadic supercell. Section 2 provides background on the Sulphur tornado and details of the data used in this study. In section 3, rapid-updating single-Doppler TVS and polarimetric radar observations are used to identify features associated with tornado dissipation. The study is summarized and put in the context of past work in section 4.

2. Data and methods

a. *Rapid X-band Polarimetric Radar and case overview*

The tornado that is the subject of this study formed northwest of Sulphur, Oklahoma, at ~2134 UTC and moved eastward for ~27 km before dissipating near Roff, Oklahoma, at ~2217 UTC according to National Weather Service (NWS) damage survey information. The tornado was rated EF3 owing to major damage to several houses (e.g., collapsed walls) at several points during the tornado's early and mature phases, in addition to debarked trees and bent electrical transmission lines (Fig. 1). The tornado inflicted approximately $4 million (U.S. dollars) worth of property damage, but fortunately there are no known fatalities despite the structures that were hit. At its widest point, the tornado was estimated to be approximately 1.5 km in diameter (see section 3a); pictures and video amassed by the NWS and the fifth author show a ''wedge'' tornado during its mature phase (not shown).

RaXPol is a mobile, rapid-scan, X-band, polarimetric radar operated by the Advanced Radar Research Center (ARRC) at the University of Oklahoma. Notable characteristics of RaXPol are a transmit frequency of 9.73 GHz, peak power of ~20 kW, and a half-power beamwidth of 1°.[1] More details can be found in Pazmany et al. (2013). There were two RaXPol deployments on the Sulphur, Oklahoma, tornado, one earlier in the tornado life cycle for ~15 min and a second deployment that captured the dissipation phase of the tornado. The second RaXPol deployment lasted from 2159:28 to 2230:58 UTC, and ended well after tornado dissipation; only data obtained in the second deployment are used in this study. For the deployment discussed herein, RaXPol scanned from 0° to 10° in elevation at 1° increments for volumetric update times of ~27–28 s. Location information of the TVS in the first RaXPol scans were used to estimate where along the path of the tornado data collection began (Fig. 1); we estimate that roughly the latter half of the tornado's path was captured. The analysis that follows focuses on the beginning of the deployment until the time of TVS dissipation at all 11 elevation angles obtained by RaXPol. Additionally, data of the mid and upper levels of the storm obtained by the WSR-88D radar in Twin Lakes, Oklahoma (KTLX), were analyzed because of RaXPol's close range to the storm and its occasional data contamination from attenuation. The distance of the storm from the KTLX WSR-88D (~85 km to the southeast) resulted in the lowest scan being approximately 1.2 km ± 150 m above ground level (AGL) (not shown).

b. *Methods*

This study is broken into two interrelated parts: analysis of the TVS and the polarimetric features of the

[1] The effective beamwidth could be as broad as 1.4° owing to beam smearing when the antenna is scanning as fast as 180° s^{-1} (e.g., Bluestein et al. 2018).

Brought to you by NOAA Central Library | Unauthenticated | Downloaded 09/15/21 06:16 PM UTC

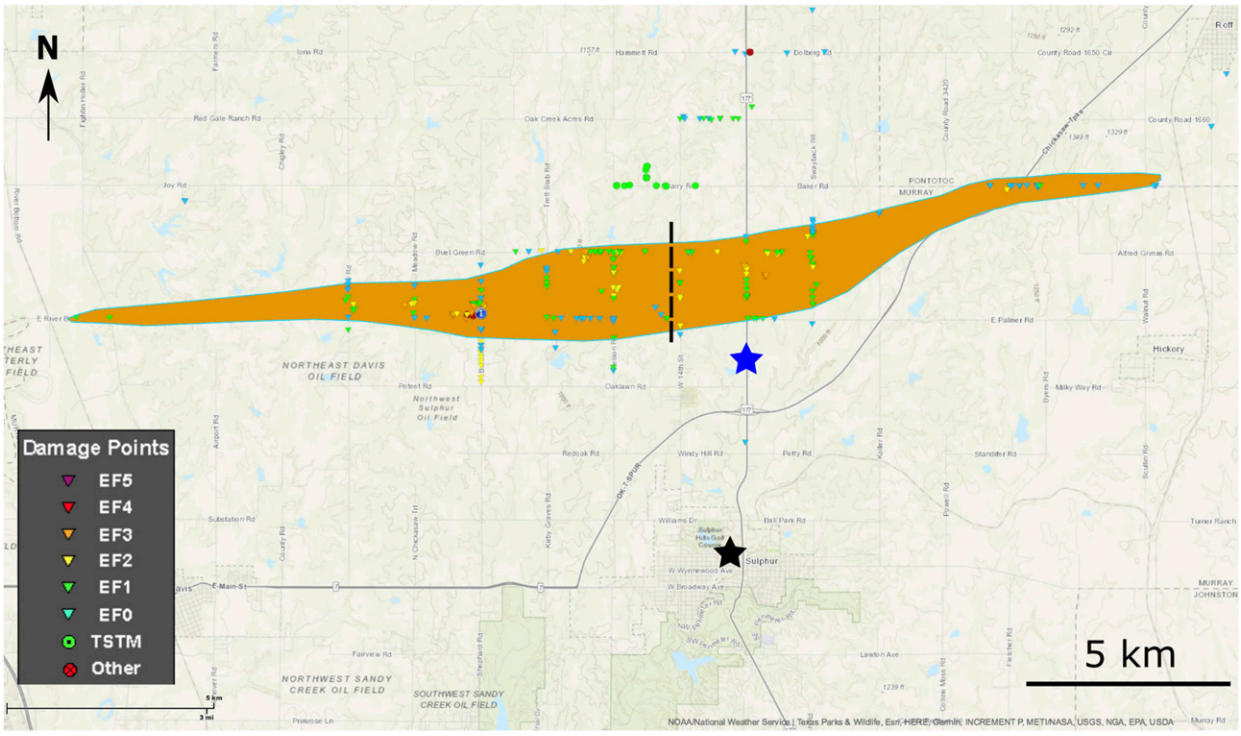

FIG. 1. The estimated pathlength, width, and intensity of the Sulphur, Oklahoma, tornado on 9 May 2016 from information compiled in the Damage Assessment Toolkit following a damage survey by the National Weather Service in Norman, Oklahoma. The orange polygon is the path area of the tornado at the surface and the triangles within it are individual damage indicator points color-coded by intensity estimated using the EF scale. The tornado was rated EF3 in accordance with the maximum damage point found. The beginning of RaXPol's deployment mapped onto the tornado path is given by the dashed black line; the end of the deployment occurred well after the tornado had dissipated. The black (blue) star indicates the approximate location of Sulphur, Oklahoma (RaXPol).

supercell. For the first part, data of the TVS[2] associated with the Sulphur tornado were manually de-aliased from 2159 to 2224 UTC using the Solo-ii (Oye et al. 1995) radar editing software (~500 individual scans). The TVS in each scan was interrogated for a variety of information (e.g., time, location, maximum inbound and outbound radial velocities) that was recorded. Tornado intensity was estimated by using the sum of the maximum inbound and outbound velocities ΔV within the TVS. Dissipation was estimated using a ΔV floor of $40\,\mathrm{m\,s^{-1}}$ (e.g., Wurman and Kosiba 2013), but because the $40\,\mathrm{m\,s^{-1}}$ ΔV threshold is arbitrary, dissipation sensitivity analyses (i.e., analyses using multiple TVS ΔV floors) also were performed (e.g., French et al. 2014). SR motion was determined using the same method as used in FK19: a 15-min running average of Z_{DR} column centroids in WSR-88D data; past studies have correlated the Z_{DR} column with the main storm updraft (e.g., Kumjian et al. 2014; Wienhoff et al. 2018). RaXPol data then were used to determine TVS motion over short time scales. Horizontal distance offset between the tornado at the surface and the midlevel updraft also was determined as in FK19: the same WSR-88D centroid of the Z_{DR} column was used as an approximation of the midlevel updraft location and the lowest-observed scans of the TVS in RaXPol data for the two inputs.

Examination of polarimetric RaXPol data was mostly qualitative. Many aspects of the tornado and its evolution were informed at least partially by analyzing copolar correlation coefficient (ρ_{HV}) data, including the size of the tornado (via TDS), when it dissipated, and how boundaries may have influenced its evolution. RaXPol's high spatial and temporal resolution data would be ideal in investigating known polarimetric signatures and determining bulk DSDs for this case. However, at multiple locations in the storm, there were

[2] The detailed structure of the winds in the tornado core flow is captured in RaXPol data owing to the short range to the tornado and its large size. Therefore, the radar representation of the tornado is a tornado signature (TS; Wood and Brown 1997). However, to prevent confusion with past studies, we refer to the tornado's representation in RaXPol data as a TVS.

Brought to you by NOAA Central Library | Unauthenticated | Downloaded 09/15/21 06:16 PM UTC

large amounts of attenuation and differential attenuation to the point of Z_H and Z_{DR} signal extinction, and correction attempts would not have been feasible. Instead, only signatures prominently identified in ρ_{HV} data (rather than Z_{DR} data) were analyzed and data from KTLX were used to estimate bulk hook echo DSDs. Fortunately, KTLX was run in the Multiple Elevation Scan Option (MESO; Chrisman 2014) mode for Supplemental Adaptive Intravolume Low-Level Scans (SAILS; Chrisman 2013). MESO-SAILS data collection allowed for the lowest-observed level of the storm to be observed by KTLX every 1.5–2 min rather than every 5–6 min.

Hook echo DSDs in KTLX data were determined almost identically to French et al. (2015a) and were based on data from Cao et al. (2008). The hook echo was subjectively detached from the main storm (forward flank region) at the location where the gradient in the width of Z_H was approximately maximized. A ρ_{HV} threshold was applied such that values < 0.97 were eliminated to mitigate hail contamination and data from within the TDS. The latter is particularly important in this case because of the large size of the TDS (see section 3b). Mean and median Z_{DR} and specific differential phase (K_{DP}), median drop size (D_0), and number concentration (N_T) changes with time were examined. To account for Z_{DR} biases, an exhaustive correction routine was applied that emulated the approach taken by the Radar Operations Center (e.g., Richardson et al. 2017). Three approaches of external target bias estimation were averaged (light rain, dry snow, and Bragg scatter signatures) using data ±48 h from the time of tornadogenesis. The averaging used a weighted mean with weights of 0.25, 0.33, and 0.42, respectively. For D_0 and N_T calculations, the methods and equations described in Cao et al. (2008) were used. Given the range of the storm from KTLX, the level the hook echo characteristics were calculated at is higher than in past studies, and may not represent conditions near the surface.

3. Observations of tornado dissipation

a. TVS characteristics

As data collection began, raw radial velocity observations and time series TVS intensity data provide strong evidence of a large and very intense tornado (ΔV of 160–190 m s^{-1}; Figs. 2a,b). In the first 3 min of RaXPol data collection, radial velocities just above the surface are consistently larger than the upper bound of 3-s gusts mapped to EF3 damage intensity (~74 m s^{-1}; Figs. 2b,c). Further, there are 14 scans within four different volumes in which radial velocity observations surpass the lower bound of 3-s gusts mapped to EF5 damage intensity (~89.5 m s^{-1}; e.g., Fig. 2b). In addition, five scans contain radial velocities > 100 m s^{-1} in the TVS (not shown)[3] and there is evidence of multiple vortices (Fig. 2b). The TVS is most intense near the surface and weaker, but only slightly so, at higher levels shortly after the deployment began. During the dissipation phase of the tornado, the intensity initially falls rapidly: ΔV decreases from ~190 to 100 m s^{-1} between 2159:30 and 2205:01 UTC (e.g., Figs. 2b–e). Over the next ~15 min, intensity declines consistently, but does so at a slower pace (e.g., Figs. 2f,g) after which it hovers for several minutes at and above typical thresholds used to define likely tornado circulations in radar data (Figs. 2h,i). Reductions in intensity proceed similarly near the surface, at ~500 m, and at ~1-km height levels (Fig. 2a). The distance between maximum inbound and outbound radial velocities in the TVS is consistently ~1–1.5 km (Figs. 2b–h) and the TVS only contracts in size just prior to dissipation (e.g., Figs. 1, 2i).

RaXPol observations of the Sulphur TVS are presented in this section to (i) estimate how the tornado dissipated in time and height and (ii) determine the short-time-scale evolution of two of the four FK19 dissipation behaviors: intensity decrease and SR rearward motion. The short time scale evolution of the other two dissipation behaviors, TVS tilt and horizontal displacement between TVS and midlevel updraft calculations, were not calculated. The short upper height bound on the RaXPol TVS domain of ~500 m (~2 km) at the beginning (end) of data collection, combined with the extremely large size of the TVS and difficulty determining an objective TVS center introduces the potential for large errors in inclination calculations, so tilt evolution is described qualitatively. Furthermore, the latter behavior requires knowledge of the midlevel updraft location, which was located beyond RaXPol's highest viewing angle. However, WSR-88D data were used to estimate the overall change in TVS-updraft horizontal displacement from the beginning of the RaXPol deployment to TVS dissipation.

[3] Climatological studies have found a much larger percentage of violent (EF4–EF5) tornadoes when near-surface mobile Doppler radar data are used to estimate tornado intensity (Alexander 2010). Though there are shortcomings to using radar data to estimate tornado intensity (Snyder and Bluestein 2014), there are several examples of large discrepancies between survey and radar data when the tornado path includes swaths of open land (e.g., Wurman et al. 2014; Wakimoto et al. 2016). Given the lack of development over parts of the Sulphur tornado path, we believe it to be highly probable that the true tornado intensity was greater than that indicated by the damage survey.

Brought to you by NOAA Central Library | Unauthenticated | Downloaded 09/15/21 06:16 PM UTC

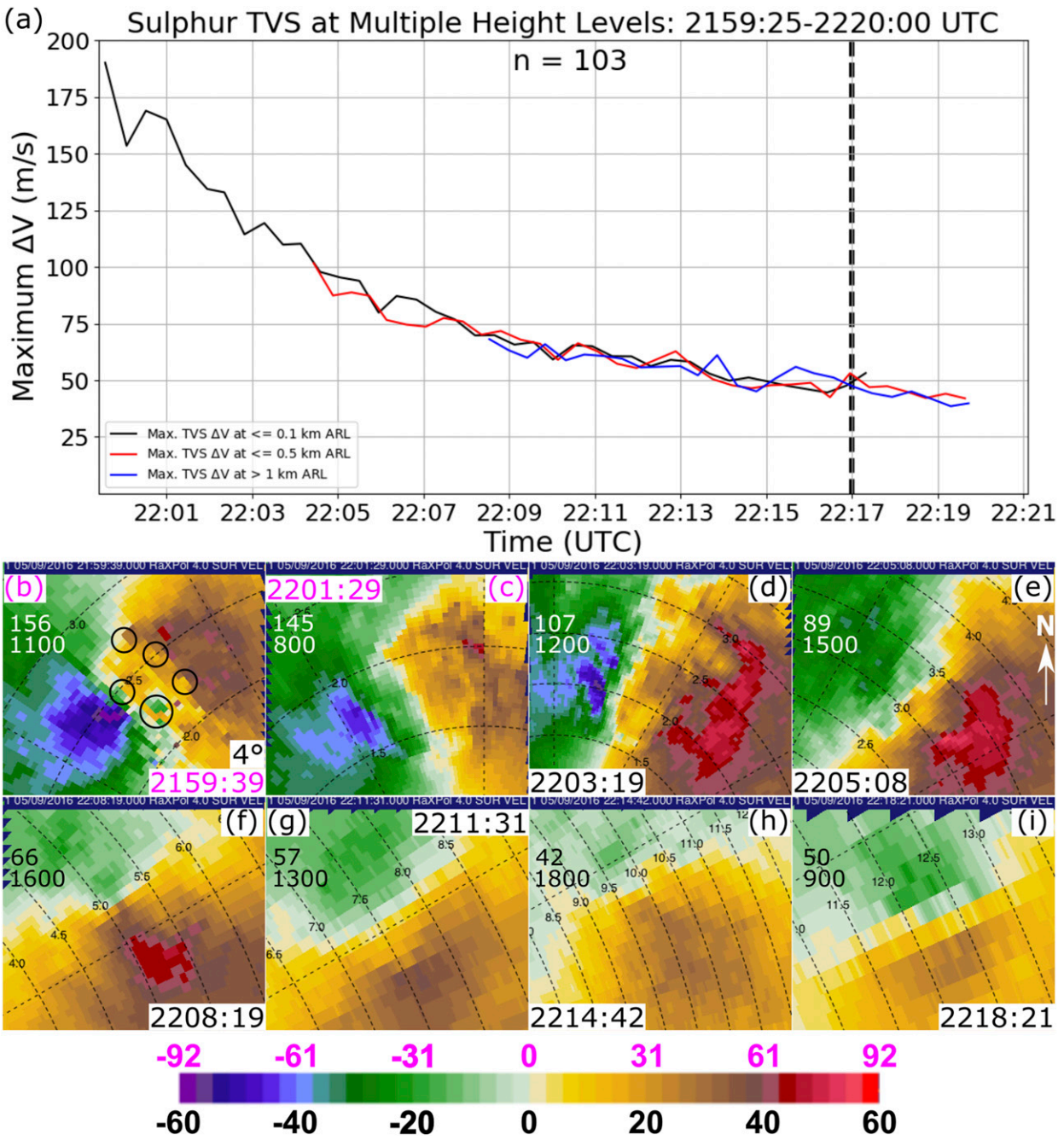

FIG. 2. TVS intensity in the Sulphur supercell shown as (a) a time series of ΔV at the center beam height closest to 100 m (black), 500 m (red), and 1 km (blue) ARL using a TVS cutoff of $\Delta V \leq 40$ m s^{-1}, and a progression of radial velocity (m s^{-1}) PPIs at 4.0° elevation angle during the life cycle of the TVS at (b) 2159:39, (c) 2201:29, (d) 2203:19, (e) 2205:08, (f) 2208:19, (g) 2211:31, (h) 2214:42, and (i) 2218:21 UTC. The dashed black line in (a) is the estimated time of tornado dissipation based on damage survey information entered in *Storm Data*. In (b)–(i), the top (bottom) number represents the maximum TVS ΔV in m s^{-1} (approximate TVS width in m rounded to nearest 100 m). In (b), evidence of multiple vortices in the tornado are enclosed by black circles and range rings are every 500 m. The large decrease in TVS intensity necessitates a change in radial velocity scale from (c) to (d), which is color coded.

Brought to you by NOAA Central Library | Unauthenticated | Downloaded 09/15/21 06:16 PM UTC

A time–height series of TVS dissipation was quantified using three ΔV thresholds (Fig. 3). The Sulphur supercell was moving away from RaXPol during the deployment, causing radar center beam heights to increase with time. However, because data collection was restricted to a maximum of 10° elevation, only the lowest ~2 km was observed at the time of tornado dissipation. In this case, using the ''standard'' ΔV threshold of 40 m s^{-1} (e.g., Wurman and Kosiba 2013), the TVS dissipates first in the RaXPol domain in the 1.5–2-km layer (Fig. 3a). Then, ~30 s later, the TVS dissipates rapidly within one to two volume scans (25–50 s) below the 1.5-km height level. The last recorded TVS observation occurs at 2220:11 UTC at a height level of ~1 km, a time that is within ~3 min of the estimated dissipation time based on the damage survey (2217 UTC). When using a less stringent TVS ΔV criterion, 35 m s^{-1} (Fig. 3b), dissipation occurs nearly simultaneously in the lowest 2 km, within one volume scan (27 s). If using a more stringent TVS ΔV criterion, 45 m s^{-1} (Fig. 3c), dissipation occurs first in the 1–2-km layer, and below that within two volume scans (~50 s). Because of the arbitrary nature of using TVS ΔV cutoffs to define TVS dissipation, we emphasize that the TVS weakens to or close to multiple plausible subtornadic thresholds first in the 1.5–2-km height layer and then dissipates quickly after that in the lowest 1.5 km. Another limitation of using ΔV in time–height analyses is the possibility of a contorted (i.e., more horizontally oriented) vortex going unobserved in radial velocity data; in this case the decline in intensity at multiple levels rapidly makes it unlikely that such an orientation bias results.

The SR motion of the Sulphur tornado was investigated using different ''integration periods'' at both ~100 and ~500 m above radar level (ARL) and using a coordinate system transformed into forward–rearward and rightward–leftward components when looking from rear to front (e.g., FK19). Small errors in TVS location of ~100 m could lead to large errors in SR motions of ~5 m s^{-1} using 30-s volumetric updates. As a result, SR motions were determined using a 2-min duration offset such that the SR motions are a running 2-min average (Fig. 4). The TVS SR motion estimated from the scans closest to 100 m ARL is mostly forward (Fig. 4a) and leftward (Fig. 4b), but with relatively small magnitudes, and the motion becomes more rearward in the final minutes prior to dissipation. *Also, both components oscillate with a period of ~4–5 min during the RaXPol deployment*; shifts to increasing forward (rearward) SR motion occur 1–2 min before shifts to more leftward (rightward) SR motion and vice versa. Some of the changes in SR motion are very large, for example from forward to rearward from 2209 to 2211 UTC (Fig. 4a).

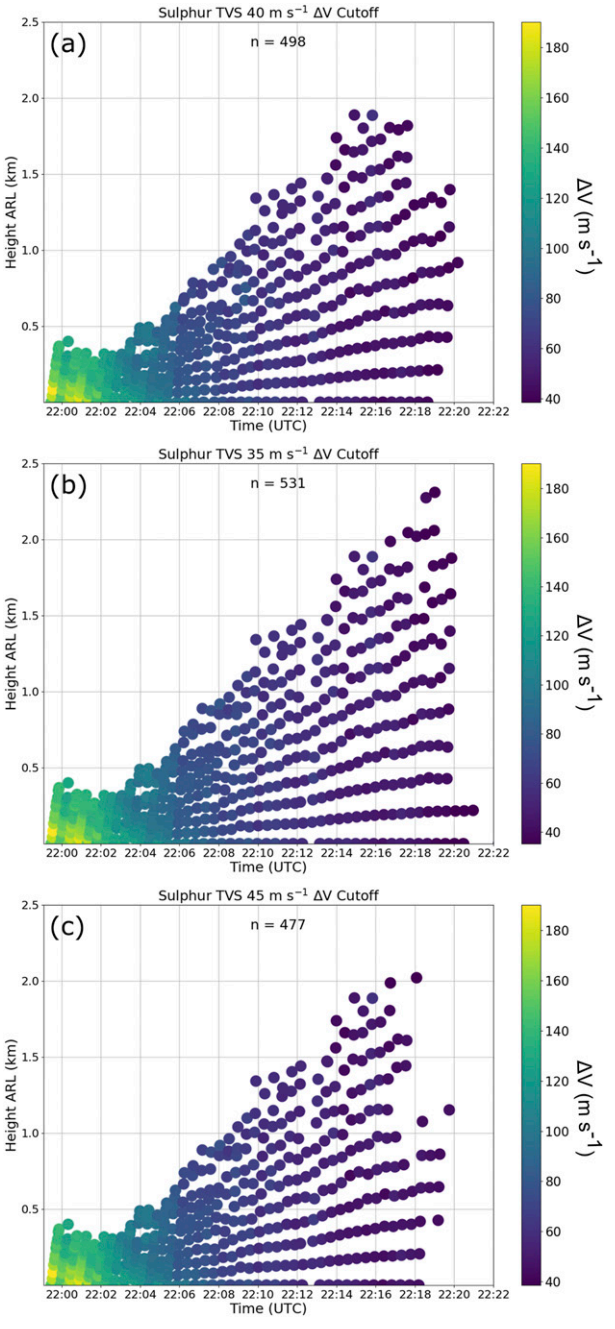

FIG. 3. TVS intensity in the Sulphur supercell represented as time–height series of TVS ΔV (m s^{-1}) from 2159:25 to 2220:10 UTC using a TVS cutoff of (a) $\Delta V \leq 40$, (b) $\Delta V \leq 35$, and (c) $\Delta V \leq 45$ m s^{-1}.

The similar SR components at both the 100- and 500-m height levels provide increased confidence of true oscillatory behavior. The 5-min running averages also are shown to roughly mimic what a WSR-88D might observe. Given that the period of the oscillations is roughly equal to the update time of the WSR-88D

Brought to you by NOAA Central Library | Unauthenticated | Downloaded 09/15/21 06:16 PM UTC

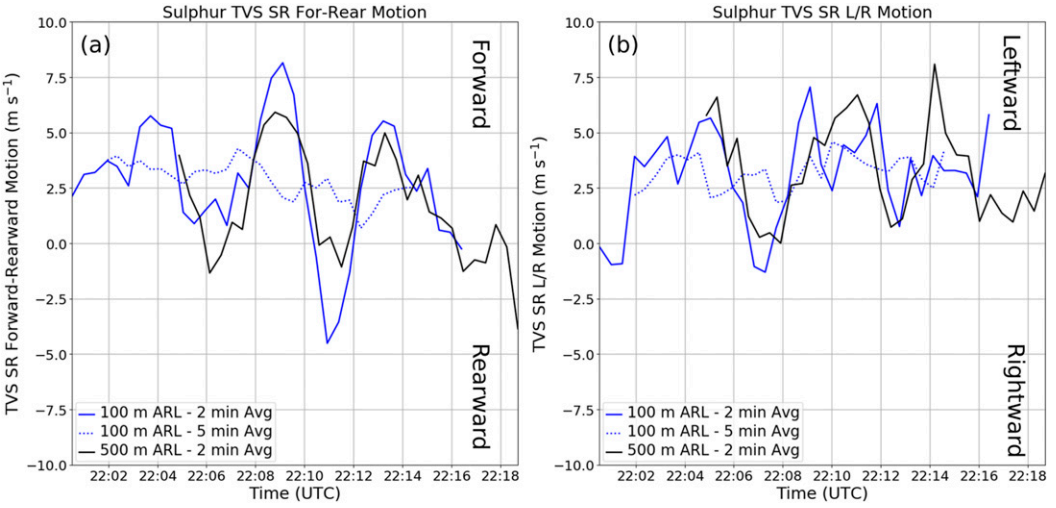

FIG. 4. Time series of SR motion (a) forward–rearward and (b) rightward–leftward components using 2-min (solid) running averages from RaXPol scans at the center beam height closest to 100 (blue) and 500 m (black) ARL. For comparison, a 5-min running average also is shown for the 100-m height data (dotted blue lines). Positive (negative) values indicate forward (rearward) and leftward (rightward) SR motion. Any data with center beam heights that were more than ±100 m from the 100- or 500-m height levels were not included in the calculations.

network (neglecting SAILS) the oscillations are severely damped and barely observable using the 5-min averages. The ground-relative track of the TVS at multiple levels (not shown) does not provide clear evidence of trochoidal motion[4] that would result from the tornado rotating about a broader mesocyclone.

Finally, regarding tilt and TVS-updraft horizontal displacement, the former field was noisy, but did show a large amount of surface to 500 m TVS tilt at the beginning of data collection that decreased rapidly at ~2202 UTC (not shown). For the latter field, KTLX Z_{DR} column data were matched to within 5 s of RaXPol TVS data at the beginning and end of the RaXPol deployment to estimate overall changes in the horizontal offset between the TVS close to the surface and the location of the midlevel updraft. The horizontal distance between the TVS and the midlevel updraft increases from ~2.2 to ~4.5 km from 2200:04 to 2219:34 UTC (not shown). As discussed previously, the lack of RaXPol Z_{DR} column data prevents an accurate examination of the evolution of the horizontal displacement over short time scales.

[4] Only small displacements of the TVS off the mesocyclone centerline (<1 km) would be needed to support trochoidal motion given the 4–5-min period of SR oscillations and SR motions of ~5 m s^{-1}. As a result, we cannot rule out trochoidal motion owing to the large size of the TVS and potential errors in our estimates of its centered locations.

b. Polarimetric observations

The lack of previous polarimetric radar studies of dissipating tornadic supercells motivates examining how signatures and DSD proxies evolved as the tornado decayed in the Sulphur supercell. In this case, there are two signatures identified for further analysis that leverage RaXPol's rapid-scan and polarimetric capabilities: a low reflectivity ribbon (LRR; Wurman et al. 2012; Kosiba et al. 2013; Snyder et al. 2013) and a TDS coincident with the tornado. In addition, we used the KTLX WSR-88D polarimetric radar data to investigate hook echo DSD proxies leading up to tornado dissipation. Other signatures not examined either occurred above RaXPol's data collection ceiling for this case (e.g., Z_{DR} column) or are obscured or partially obscured in RaXPol data because of differential attenuation (e.g., Z_{DR} arc).

Easily identifiable at the very beginning of the RaXPol deployment is a prominent LRR (Fig. 5). The LRR appears as large reductions in reflectivity and differential reflectivity of 30–40 dBZ and 3–4 dB, respectively, and also is apparent as a ρ_{HV} deficit, ranging from > 0.95 directly outside of it to 0.3–0.8 coincident with the Z_H and Z_{DR} reductions (Fig. 5a). The LRR is identifiable at all levels in RaXPol data (lowest ~1.2 km ARL at 2200 UTC) for several minutes until it becomes less distinct after ~2206 UTC (Fig. 5b) and is difficult to discern after ~2208 UTC (Fig. 5c); the LRR is likely still a real feature at these times, but attenuation and differential attenuation in the "spine" of the hook echo

Brought to you by NOAA Central Library | Unauthenticated | Downloaded 09/15/21 06:16 PM UTC

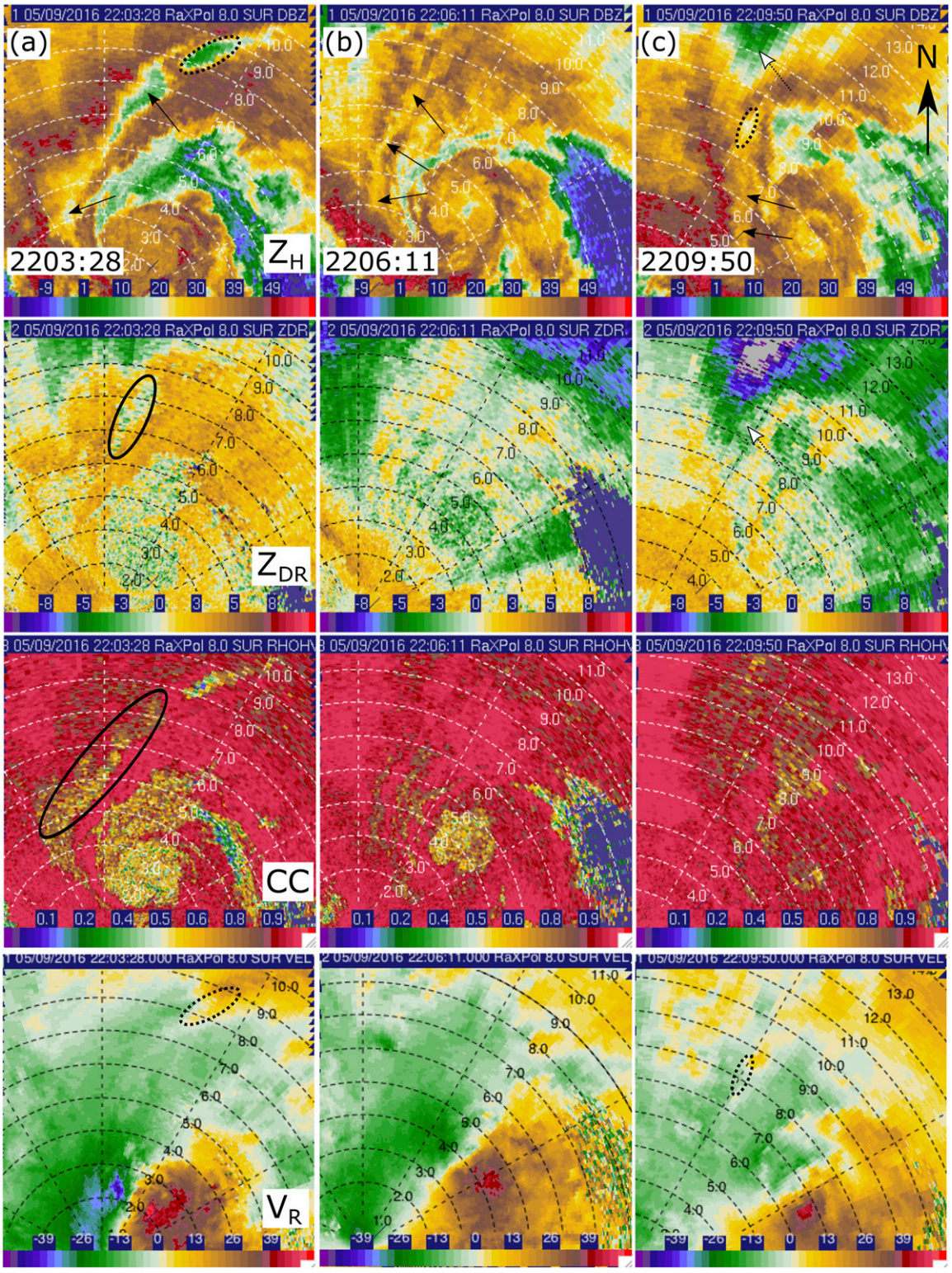

FIG. 5. RaXPol PPIs at 8.0° elevation angle from (a) 2203:28, (b) 2206:11, and (c) 2209:50 UTC 9 May 2016 of (top) radar reflectivity (dBZ), (second row) differential radar reflectivity (dB), (third row) copolar correlation coefficient, and (bottom) radial velocity ($m\ s^{-1}$). The black arrows in the top panels point to the LRR, the white arrows in (c) point to attenuation and differential attenuation in radar reflectivity and differential radar reflectivity, the solid black ovals in the second and third rows of (a) identify deficits in differential reflectivity and copolar correlation coefficient, respectively, within an LRR patch, and the dotted black ovals in (a) and (c) identify patches of the LRR associated with radial divergence. Range rings are every 1 km. The approximate center beam height at the location of the LRR in (a)–(c) range from 500 m to 1.2 km.

Brought to you by NOAA Central Library | Unauthenticated | Downloaded 09/15/21 06:16 PM UTC

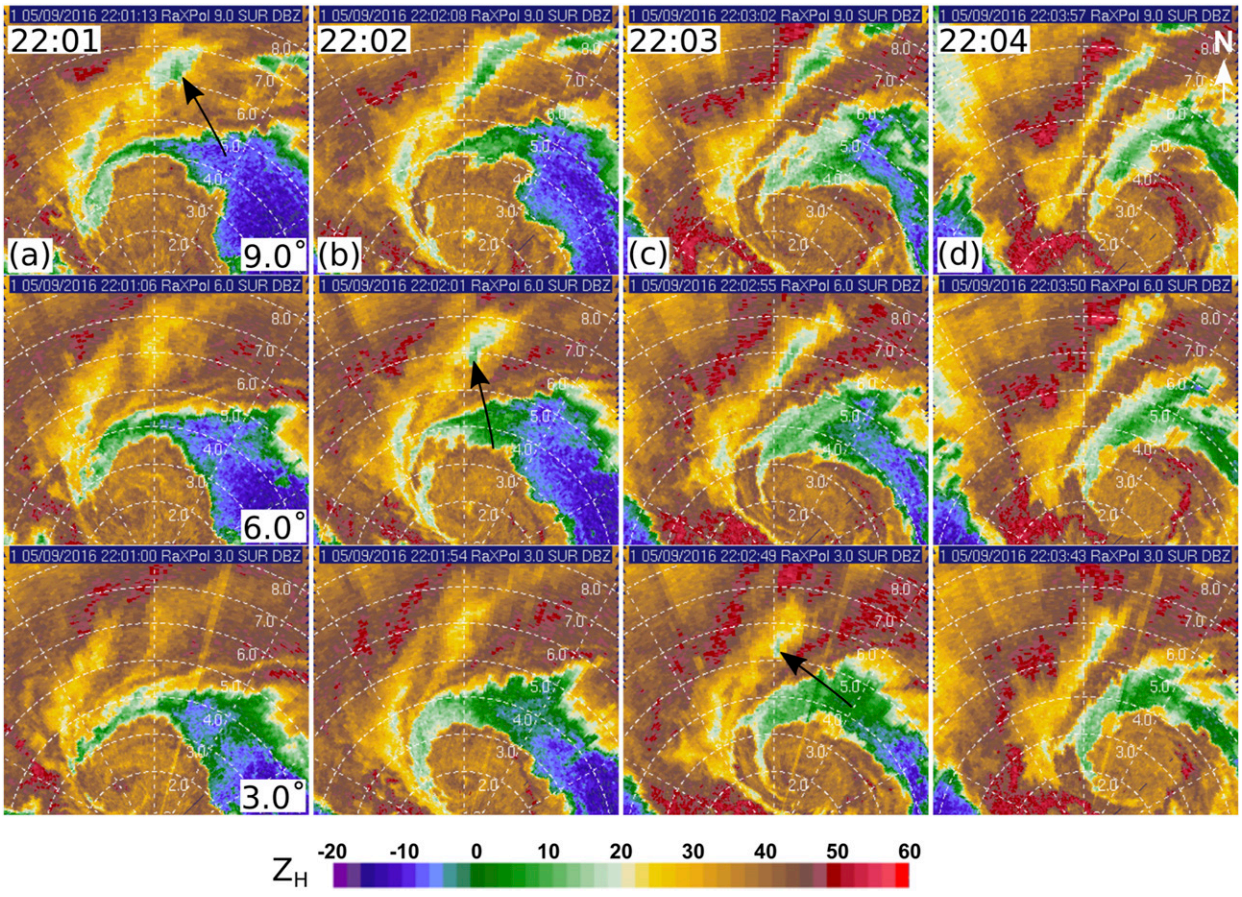

FIG. 6. RaXPol radar reflectivity (dBZ) at approximately (a) 2201, (b) 2202, (c) 2203, and (d) 2204 UTC 9 May 2016 at (top) 9.0°, (middle) 6.0°, and (bottom) 3.0° elevation angle. The first appearance of the local minimum in Z_H at each elevation angle is annotated by a black arrow. Range rings are every 1 km. RaXPol center beam heights at 9.0°, 6.0°, and 3.0° at the range of the LRR are ~1.0 km, 650 m, and 300 m ARL, respectively.

(annotated in Fig. 5c) prevent its identification. As data collection begins, the LRR is made up of two to three individual ''patches'' of Z_H deficits (e.g., Fig. 5a) that then ''fill in'' along a line (Fig. 5b). The LRR consistently extends from the hook echo to just inside the inner edge of the forward flank reflectivity gradient, but the northern part of the LRR does display some SR rearward motion during its life cycle, such that the orientation changes from northeast–southwest to north–south (Figs. 5a,c). The reduced ρ_{HV} and Z_{DR} coincident with the LRR is consistent with the presence of hail, either as small amounts of large hail or as a mix of hail and raindrops shed from melted hail (e.g., Griffin et al. 2018). At times, there is radial divergence associated with some parts of the LRR (Figs. 5a,c), though often the radial velocity field is difficult to interpret over the small region the LRR encompasses. In addition, the LRR is subtle in KTLX data: there is a ~5-dBZ reduction in Z_H, no observable change in ρ_{HV}, and the effects of differential attenuation are to make the Z_{DR} field ambiguous (not shown). The lack of a LRR in KTLX data likely derives from inferior KTLX spatial resolution at ~80-km range.

The rapid volumetric updates in the lowest 1 km ARL from RaXPol data afford an opportunity to observe how the LRR evolves in time and height as it becomes more apparent from 2200 to 2204 UTC (Fig. 6). One of the aforementioned patches of Z_H deficits is already present at the top of RaXPol's domain at the start of data collection, but not in the lowest ~500 m ARL (e.g., middle and bottom panels in Fig. 6a). Over the next few minutes, there is a clear progression downward of the LRR local Z_H minimum from ~1 km to ~600 m ARL first (Fig. 6b) and then down to ~300 m ARL (Figs. 6c,d). Eventually the minimum reaches the lowest-observed levels, parts of which are occasionally obscured by beam blockage (not shown). Likewise, there also is a downward progression of Z_{DR} and ρ_{HV} minima during this

Brought to you by NOAA Central Library | Unauthenticated | Downloaded 09/15/21 06:16 PM UTC

time (not shown). To quantify the descent of the LRR minimum,[5] time series of the lowest Z_H value in the LRR were constructed for the three elevation angles from 2201 to 2205 UTC (Fig. 7). The Z_H minimum displayed in Fig. 6 occurs at ~1 km one (three) volume(s) before it appears at ~650 (~300) m, consistent with a decrease in Z_H that progresses rapidly downward to the surface.

The most prominent and consistent polarimetric signature in the RaXPol dataset is the large TDS coincident with the Sulphur tornado (Fig. 8). The TDS is identifiable most consistently as low values in ρ_{HV} (0.3–0.7) coincident with the TVS (Fig. 8, bottom panels). The TDS also is associated with low values of Z_{DR} at and slightly below 0 dB (Figs. 8a,b, middle panels), though there likely is differential attenuation contamination at later times (Figs. 8c,d, middle panels). In Z_H, the TDS initially is associated with a larger area of enhanced Z_H (45–50 dBZ) surrounding a much smaller (~200-m diameter) Z_H weak-echo hole (5–15 dBZ) near the center of the TDS (Figs. 8a,b, top panels). As data collection begins, the main core of the TDS is ~1 km in diameter at 150 m ARL (Fig. 8a) to ~1.75 km in diameter at ~400 m ARL (Fig. 8b), and beam blockage initially obscures the TDS below ~150 m ARL. The general TDS structure begins to change at ~2208 UTC. From ~2208–2210 UTC, the TDS rapidly becomes smaller and more poorly defined ($\rho_{HV} > 0.9$) first at the top of the RaXPol domain (~1.3 km) down to ~300 m (e.g., Fig. 8c). The eradication of the TDS progresses downward with time to below ~300 m, but more slowly than it does above ~300 m; by ~2215 UTC, the TDS at 0.0° elevation angle also is poorly defined (Fig. 8d).

The rapid erosion of the TDS near the surface is shown in more detail in Fig. 9. Between ~2210 and 2213:30 UTC (Figs. 9a–h), the TDS is still easy to identify and large (~1–1.5 km in diameter), and is accompanied by a spiral band of reduced ρ_{HV} that likely represents rapid ingestion of inflow environmental air (see subsequent discussion). However, beginning at 2214:04 UTC (Fig. 9i), there is a near-simultaneous reduction in the diameter of the TDS and in the visibility of the low ρ_{HV} band. For the next 90 s (Figs. 9j–l), the TDS diameter stays approximately constant, after which it again erodes rapidly (Figs. 9m–o) such that there is no longer an easily identifiable organized TDS associated with the TVS (e.g., Fig. 9p).

[5] LRR descent is illustrated using a Z_H point measurement at each time and radar level. As a result, a calculated "LRR descent velocity" may be quite different from hydrometeor fall speeds. The latter is best estimated using directly observed or retrieved vertical velocities.

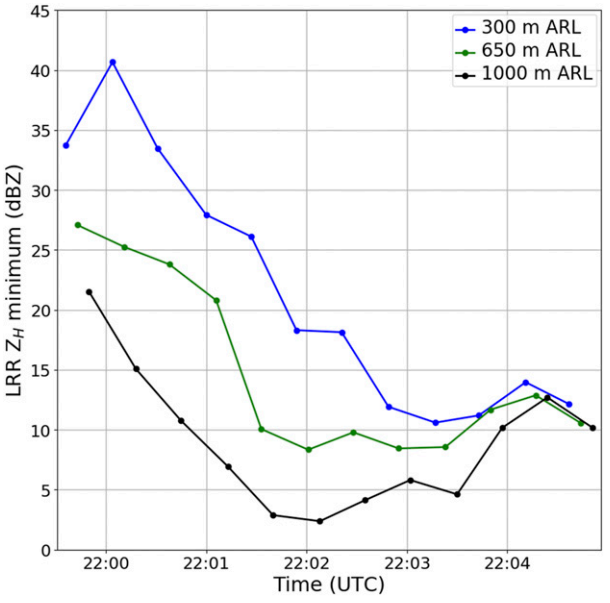

FIG. 7. Time series of the local minimum of radar reflectivity (dBZ) in the Sulphur supercell LRR at 9.0° (black), 6.0° (green), and 3.0° (blue) elevation angle. The approximate RaXPol center beam height at the range of the LRR is 1 km, 650 m, and 300 m, respectively.

In this case, spiral bands emanating from the main TDS are common at all observed RaXPol levels (e.g., Fig. 10). Spiral bands have been observed adjacent or connected to the TVS or TDS in previous studies associated with (i) low-level ingestion of environmental air by the updraft/tornado (e.g., Kumjian and Ryzhkov 2008) and (ii) apparent debris "ejections" from the TDS hypothesized to be caused by internal RFD momentum surges (Kurdzo et al. 2015; Houser et al. 2016). The internal RFD momentum surges sweep debris out of the TDS or, perhaps more likely owing to convergence at their leading edge, mark an accumulation of debris fallout in regions of enhanced descending air. In this case, however, one of the spiral bands has origins that may be different from others previously documented. At several times, a comma-shaped band of reduced Z_H, ρ_{HV}, and Z_{DR} extends from south of the TDS and connects continuously with the aforementioned reduced values identified as a LRR; in other words, *the LRR feeds directly into the TDS* (Fig. 10a). To our knowledge, this is the first documentation of a LRR that connects directly to the approximate location of a tornado. At other times, the reduced ρ_{HV} coincident with the LRR is separated from the main TDS (Fig. 10b).

Other spiral bands of reduced ρ_{HV} are located off the western or southwestern flank of the TDS wrapping cyclonically around the main TDS into the storm inflow layer (Figs. 10a,b) and located from off the southern

Brought to you by NOAA Central Library | Unauthenticated | Downloaded 09/15/21 06:16 PM UTC

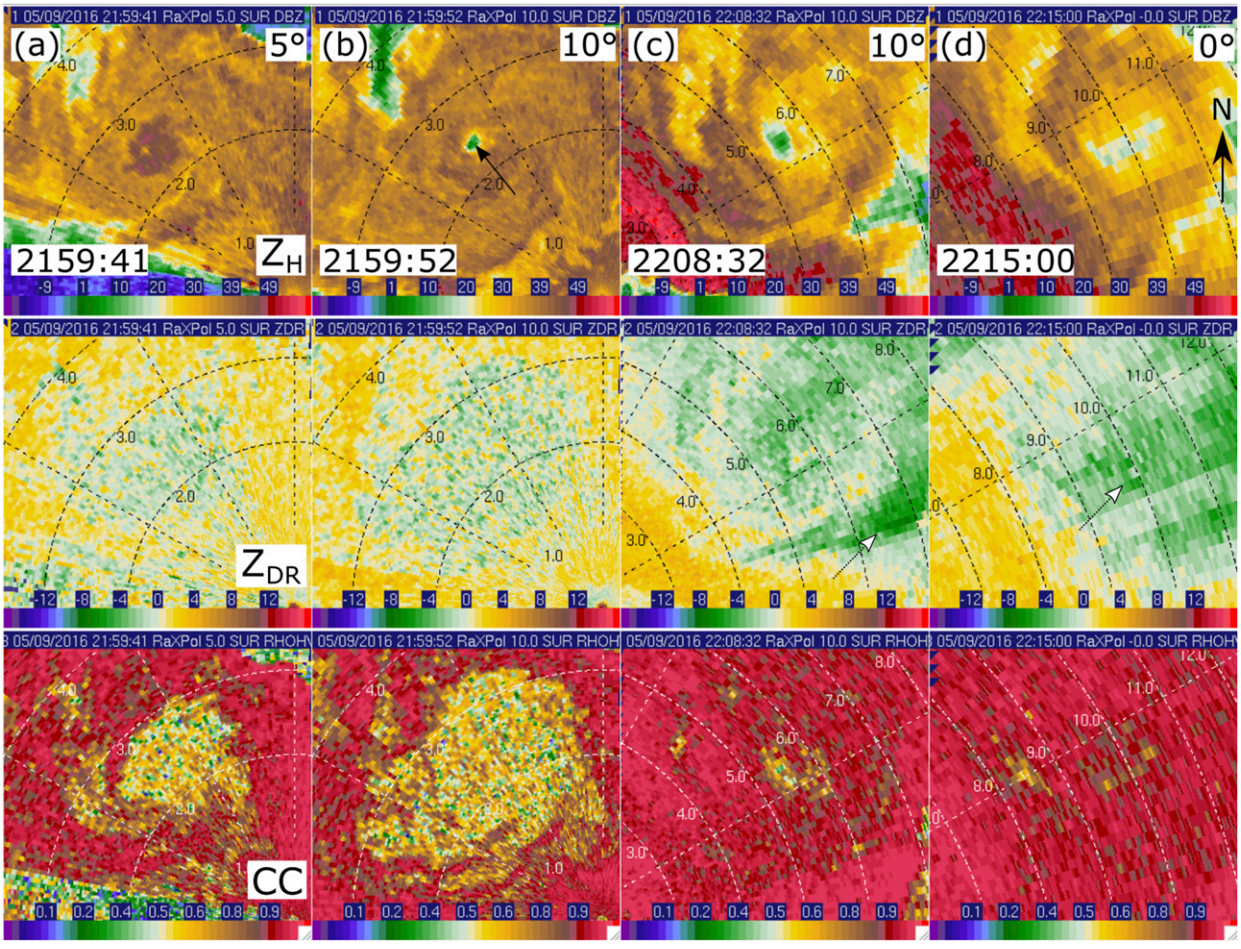

FIG. 8. RaXPol PPIs from (a) 2159:41, (b) 2159:52, (c) 2208:32, and (d) 2215:00 UTC 9 May 2016 of (top) radar reflectivity (dBZ), (middle) differential radar reflectivity (dB), and (bottom) copolar correlation coefficient. The black arrow in (b) points to a small area of reduced Z_H within the TDS and the white arrows in (c) and (d) indicate likely areas of differential attenuation. Range rings are every 1 km. PPIs in (a) and (b) are centered in the same location. The approximate center beam height at the location of the TDS in (a)–(d) are 200 m, 400 m, 1 km, and near the surface, respectively.

portion of the main TDS extending southward and periodically moving from west to east (Fig. 10b). The former band is present for most of the duration of the TDS. Given the reduced Z_H coincident with the spiral band and its continuous extension to outside the storm, the band likely represents strong inflow being ingested by the tornado containing a large amount of dust, insects, and other nonmeteorological scatterers. The latter spiral band is intermittent and highly variable in spatial extent and evolution. Initially, it is associated with low Z_H like the other two bands, but later is not (not shown). Its location is consistent with the aforementioned debris ejections in concert with an internal RFD momentum surge documented in other studies (Kurdzo et al. 2015; Houser et al. 2016), but it does not expand outward away from the tornado (not shown) as in other cases. Another possibility is that it is simply an extension of the inflow band. A more conclusive example of a debris ejection and possible internal RFD momentum surge from ~5 min earlier is discussed at length in section 4.

Polarimetric data also were used to determine if there are changes in bulk DSDs in the hook echo of the supercell during the late mature and dissipation phases of the tornado. During this period, numerous oscillations in the polarimetric variable and retrieved DSD quantities are present. The tornado dissipates during a period of substantial increase in mean and median drop size and Z_{DR} (Figs. 11a,b). However, similar increases in Z_{DR} and D_0 are observed from 2157 to 2203 UTC, during the initial rapid decrease in TVS intensity, and the tornado persists for another ~15 min. In addition, there also is an increase in K_{DP} (Fig. 11c) just prior to dissipation; K_{DP} is related both to drop shape, as in Z_{DR}, but also N_T. The latter variable also increases in the

Brought to you by NOAA Central Library | Unauthenticated | Downloaded 09/15/21 06:16 PM UTC

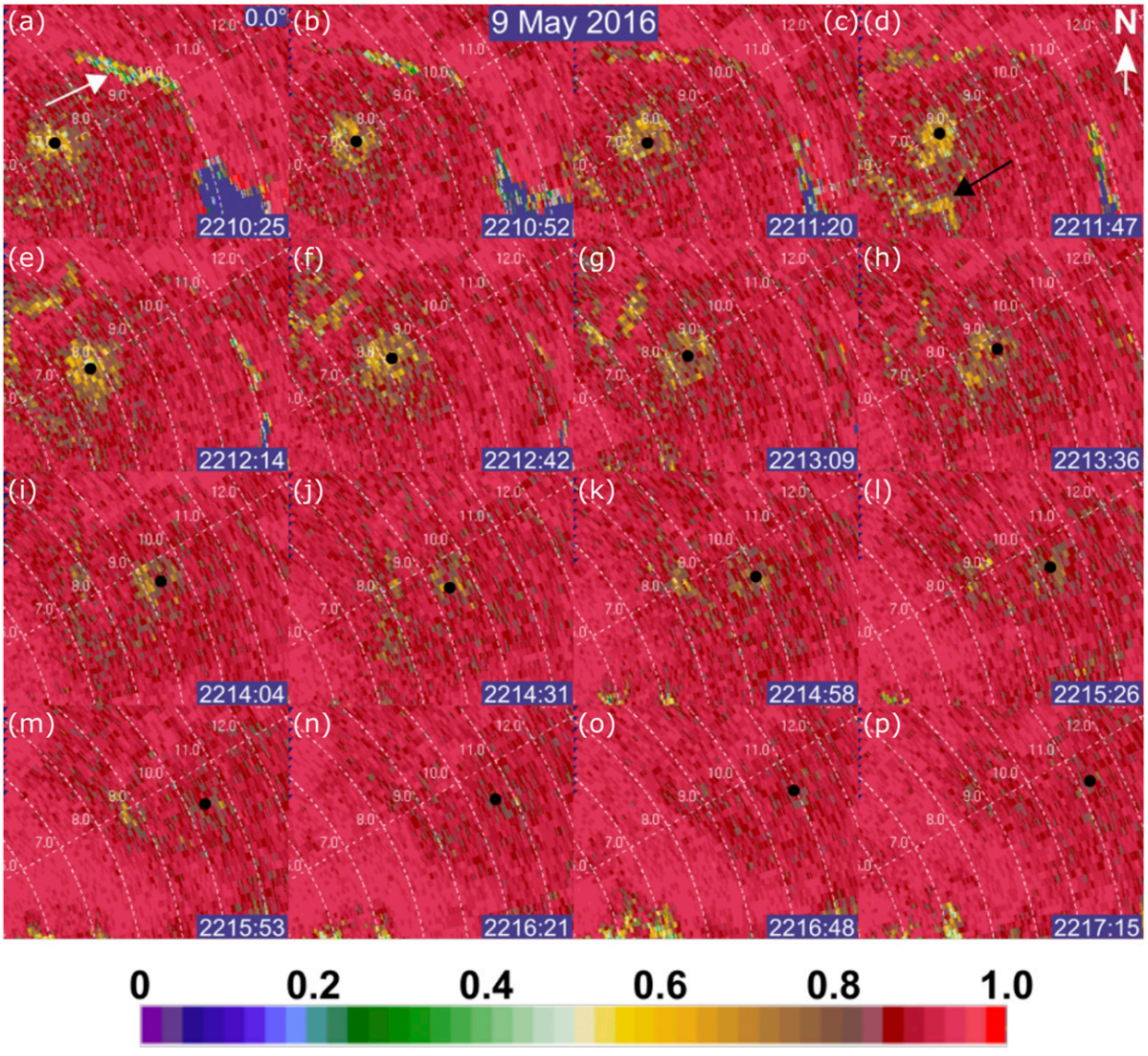

FIG. 9. Copolar correlation coefficient at 0.0° elevation angle showing the progression of the TDS associated with the Sulphur TVS at (a) 2210:25, (b) 2210:52, (c) 2211:20, (d) 2211:47, (e) 2212:14, (f) 2212:42, (g) 2213:09, (h) 2213:36, (i) 2214:04, (j) 2214:31, (k) 2214:58, (l) 2215:26, (m) 2215:53, (n) 2216:21, (o) 2216:48, and (p) 2217:15 UTC. The white and black arrows point to a region of reduced values that likely result from ingestion of storm inflow. The black circles mark the approximate center of the TVS. Given the 0.0° elevation angle, data at the location of the TDS originate in the lowest approximate 150 m ARL layer.

hook echo during the dissipation phase (Fig. 11d). Both K_{DP} and N_T increase again after displaying intermittent oscillatory behavior, the previous increases occur between 2157 and 2203 UTC. The increases in all four quantities shown are consistent with periodic influxes of larger drops and/or a larger number of nonspherical drops during the dissipation phase, including during the initial rapid intensity decrease and prior to TVS dissipation. However, recall that the reduction in TVS intensity is monotonic leading up to dissipation, so there is not an obvious direct relationship between TVS intensity and the polarimetric fields. We also emphasize again that polarimetric retrievals occur at 1.5 km ARL and there may be differences in values close to the surface. Also, the use of KTLX data and the relatively high initial scan levels prevent a detailed look at how these variables progressed vertically over short time scales.

4. Summary and discussion

Many of the observations discussed in section 3 are consistent with observations from previous tornadic

Brought to you by NOAA Central Library | Unauthenticated | Downloaded 09/15/21 06:16 PM UTC

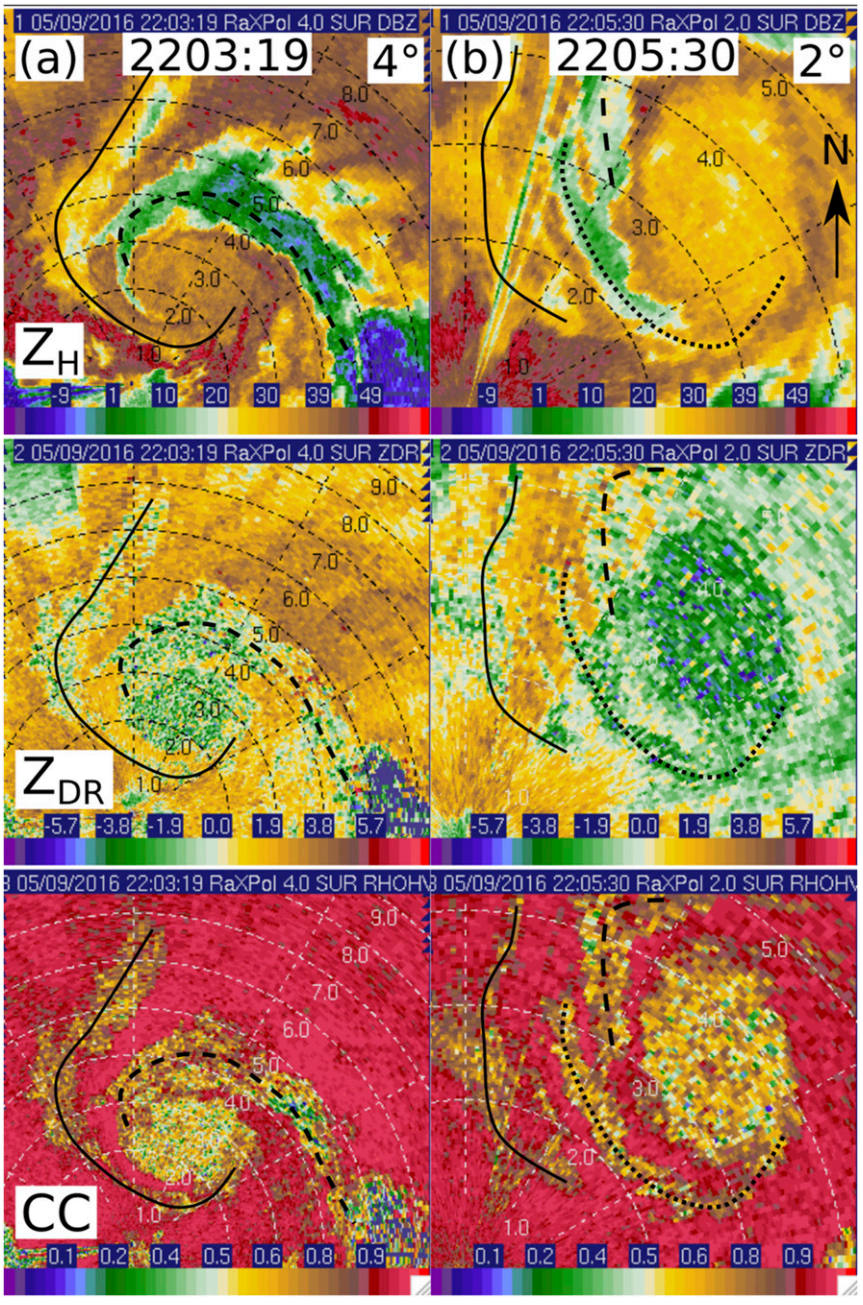

FIG. 10. RaXPol PPIs from (a) 2203:19 UTC at 4.0° elevation and (b) 2205:30 UTC at 2.0° elevation on 9 May 2016 of (top) radar reflectivity (dBZ), (middle) differential radar reflectivity (dB), and (bottom) copolar correlation coefficient. Annotated as black lines are three bands observed attached to or in the vicinity of the main TDS that are associated with the LRR (solid line), the storm inflow/rear-flank gust front (dashed line), and a band with unknown origin, possibly an extension of storm inflow or debris ejection from an internal RFD momentum surge (dotted line). Note that the PPIs in (b) are zoomed in more than in (a). The approximate center beam height at the location of the TDS in (a) and (b) are 175 and 130 m, respectively.

supercell studies. The Sulphur tornado dissipated as SR rearward motion accelerated (e.g., Dowell and Bluestein 2002a; FK19), the tornado became more horizontally displaced from the main storm updraft (e.g., Dowell and Bluestein 2002b; Marquis et al. 2012; FK19), and as hook echo Z_{DR} increased (French et al. 2015a). A LRR was observed for a period of several minutes as a tornado was ongoing, likely represented

Brought to you by NOAA Central Library | Unauthenticated | Downloaded 09/15/21 06:16 PM UTC

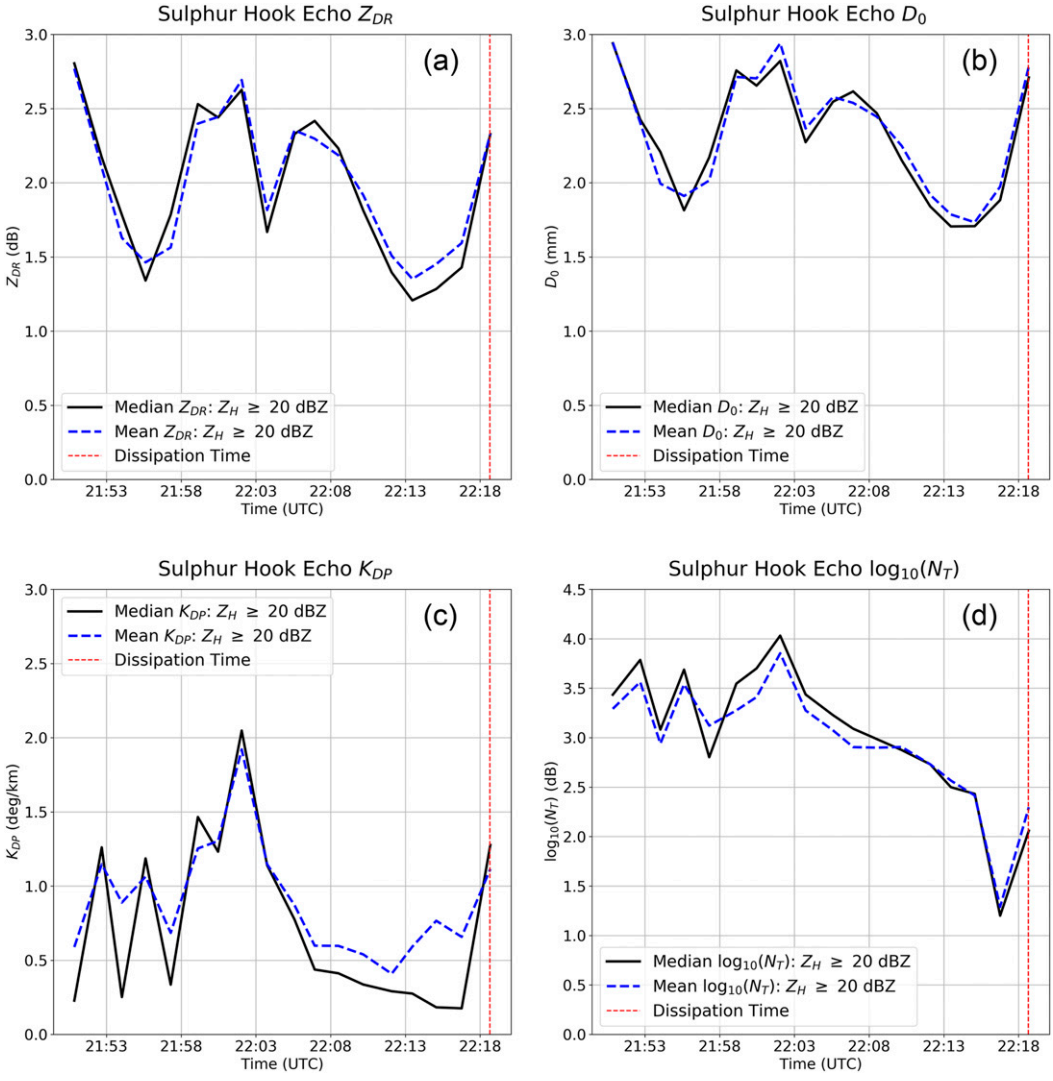

FIG. 11. Time series of median (black solid) and mean (blue dashed) (a) Z_{DR}, (b) D_0, (c) K_{DP}, and (d) logarithmic drop number concentration for the hook echo during the late mature and dissipation phases of the Sulphur tornado retrieved from KTLX data. The hook echo median center beam height is approximately 1200 ± 150 m AGL. The vertical red dashed line denotes the time of dissipation determined from the time of the last TVS at the lowest elevation angle from RaXPol data.

sparse concentrations of large hail or a mix of rain and hail, and evolved in a top-down manner (e.g., Griffin et al. 2018). Finally, a large TDS was coincident with the tornado, including several comma-shaped bands, that became less identifiable in a top-down pattern as the tornado weakened (e.g., Houser et al. 2016); the TDS then eroded rapidly in the ~5 min prior to tornado dissipation.

However, other observations are less common. The TVS dissipated rapidly, nearly simultaneously, in the lowest ~1 km using multiple TVS thresholds, contrary to TVS dissipations documented in French et al. (2014) and Houser et al. (2016), though similar to the case observed in Griffin et al. (2019). There was no evidence of short time scale TVS intensity oscillations as in French et al. (2014). The decrease in intensity in the final ~10 min was monotonic, but SR TVS motion and hook echo Z_{DR} and K_{DP} *did* portray an oscillatory structure, including before dissipation. Also unique was the consistent reduction in ρ_{HV} coincident with the LRR and its periodic connection directly to the TDS. Though we lack sufficient data to determine the thermodynamic and buoyancy characteristics of LRR air in this case, the LRR observations provide evidence that in some cases, air flowing through the LRR may feed directly into the low-level storm updraft and/or tornado.

Brought to you by NOAA Central Library | Unauthenticated | Downloaded 09/15/21 06:16 PM UTC

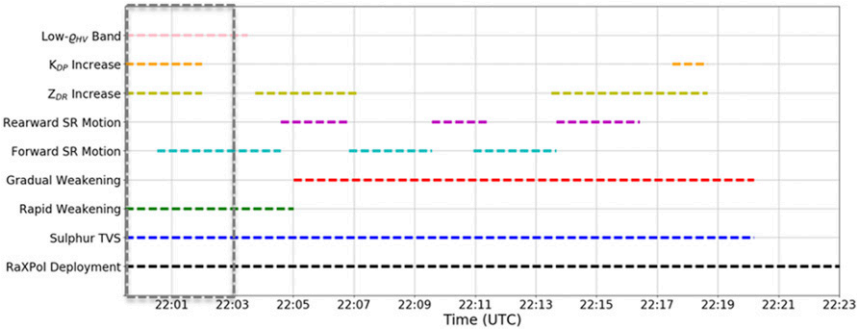

FIG. 12. A timeline of RaXPol and KTLX observations of the Sulphur tornadic supercell. From bottom to top along the *y* axis, the labeled events are the RaXPol second deployment, Sulphur TVS life cycle, rapid decline in TVS intensity, gradual decline in TVS intensity, periods of forward SR motion of the TVS and rearward SR motion of the TVS, periods when median hook echo Z_{DR} and K_{DP} increased, and a time when a band of reduced copolar correlation coefficient, likely associated with an internal RFD momentum surge, swept through the hook echo. The dashed gray box denotes the time period of interest discussed in section 4. The RaXPol deployment extended until ~2232 UTC, beyond the end time of the timeline.

A timeline of several observations during the dissipation phase of the tornado is shown in Fig. 12. Of particular interest in this case are the numerous fields that undergo regular oscillations. We believe one period of storm evolution in particular warrants more analysis is that from ~2200–2203 UTC. During the 3-min period, a number of ostensibly unrelated events occurred (Fig. 12): TVS intensity decreased rapidly (Fig. 2d), TVS SR motion became more forward (Fig. 3), and there were large increases in hook echo median Z_{DR}, D_0, K_{DP}, and N_T (Fig. 9). However, though intensity continued to decrease after this period, all of the other features reversed. It is worth addressing the question: ''Was there a common internal storm mechanism contributing to all of these short-time-scale changes?''

Recall that during the dissipation phase of the tornado, bands of reduced ρ_{HV} south of the TDS occasionally swept eastward (e.g., Fig. 10b) consistent with previously documented debris ejections. In RaXPol data, one of the aforementioned low-ρ_{HV} bands[6] does move eastward during the 2200–2203 UTC period; *it is also the largest and most well-defined band of the several observed during the RaXPol deployment* (Fig. 13). The band is identifiable as data collection began (Fig. 13a) and moves eastward (both ground-relative and SR) through the southern portion of the hook echo (Fig. 13b). The band is at its largest from 2200 to 2201 UTC with a maximum diameter of ~1.25 km as it continues to move eastward (Figs. 13c,d). Beginning at 2201 UTC, the band is more discontinuous with several adjacent pockets of reduced ρ_{HV} (Figs. 13e,f). Finally, as the band approaches the eastern edge of the hook echo, it again takes on a more linear appearance, but is much narrower than at earlier times (Figs. 13g,h).

The lack of dual-Doppler analyses[7] for this case complicates efforts to definitively identify what the feature represents. Given previous observations of debris ejections, other radar fields were examined for evidence that the low-ρ_{HV} band's origin is an internal RFD momentum surge (Fig. 14). Outside of reduced ρ_{HV}, the feature is most consistently associated with increases in spectrum width of 3–4 m s^{-1} across the band (e.g., Figs. 14a,b). Previous studies have documented increases in spectrum width in RFD primary and secondary gust-front surges (e.g., Spoden et al. 2012; Bluestein et al. 2019). For much of its life cycle, the position of the low-ρ_{HV} band relative to RaXPol is such that radial winds from an internal RFD momentum surge would be expected to be largely normal to the radar beam as the band moves east. However, early in data collection, there are radial velocity gradients consistent with radial convergence associated with the band as well; for example, from 2200 to 2201 UTC, there are local increases of ~10–15 m s^{-1} (e.g., Figs. 14c,d) coincident

[6] The timeline in Fig. 12 only includes the initial well-defined low-ρ_{HV} band discussed in section 4. The evolution of the other bands was more complex and the determination of objective begin and end times are prone to large error.

[7] Though data from KTLX are available for this case, for most of the RaXPol deployment, the lowest-observed level from KTLX is higher than the highest-observed level from RaXPol.

Brought to you by NOAA Central Library | Unauthenticated | Downloaded 09/15/21 06:16 PM UTC

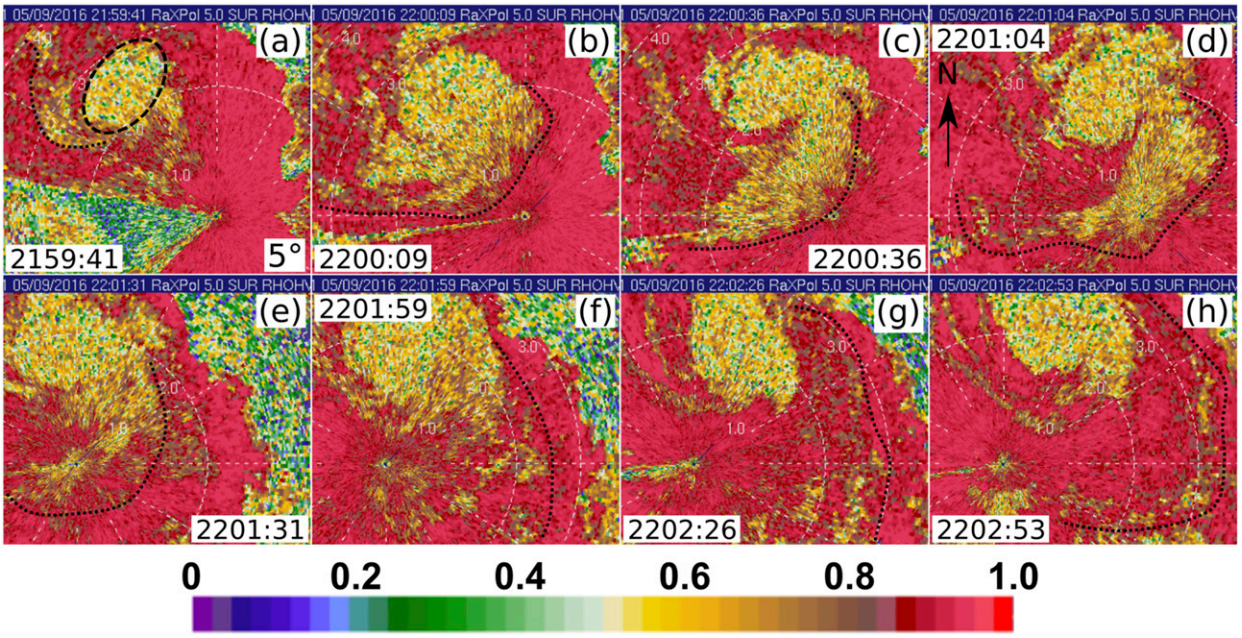

FIG. 13. RaXPol PPIs of copolar correlation coefficient at 5.0° elevation angle from (a) 2159:41, (b) 2200:09, (c) 2200:36, (d) 2201:04, (e) 2201:31, (f) 2201:59, (g) 2202:26, and (h) 2202:53 UTC 9 May 2016. Range rings are every 1 km. The outer edge of reduced copolar correlation coefficient associated with the bands are approximated with a dotted line. The outline of the main TDS is outlined by a dashed line in (a). The images are centered at the same location for (a)–(d) and (e)–(h). The approximate center beam height at the location of the TDS ranges from ~150 to 200 m.

with the low-ρ_{HV} band.[8] At other times, radar reflectivity is as much as 20 dBZ larger within the low-ρ_{HV} band (e.g., Figs. 14a,e), consistent with increased precipitation within the feature. The band also passed through the RaXPol deployment location, a time when the fifth, sixth, and seventh authors observed a large amount of debris fall out at the radar site. Based on all of the available radar and visual evidence, we hypothesize that the reduced ρ_{HV} band represents a debris ejection that results from an internal RFD surge.

We therefore speculate about one possible storm evolution scenario that ties together all the observations in this case: a strong internal RFD momentum surge advected the tornado eastward (forward in SR sense). The strong forward motion near the surface caused the tornado to become increasingly tilted toward the west with increased height (not shown) and displaced the tornado at low levels from the main storm updraft; these behaviors have previously been associated with tornado dissipation and may have contributed to a large and rapid decrease in tornado intensity during this time period. At the same time, the surge contributed to a well-defined debris ejection.

Once the internal momentum surge caught up to the primary rear-flank gust front, the aforementioned behaviors were reduced or reversed. Though it is less clear, subsequent internal RFD momentum surges may have contributed to further decreases in intensity and tornado dissipation. For example, a well-defined rear-flank gust front is observed to surge forward far ahead of the tornado between 2208 and 2210 UTC (not shown) at a time when there is a large increase in SR rearward motion (Fig. 4) and decrease in the size of the TDS (e.g., Fig. 8c).

Several aspects of the band resemble those seen in a case study of several debris ejections presented by Kurdzo et al. (2015). The ENE orientation of the band at some times (e.g., Fig. 10c) is identical to one in their case (see their Fig. 13). In their case, they also observed a large decrease in TVS intensity and an increase in forward speed during the time the band was observed. They hypothesized that an internal RFD momentum surge led to a ''failed occlusion'' that allowed for tornado maintenance to continue for an additional 12 min, roughly the same amount of time the Sulphur tornado persisted after the band passed through the hook echo. In this case, there is no evidence in the track of the TVS at low levels (not shown) or in the damage survey (Fig. 1) of any type of ''kink'' in the path that would be consistent with a failed occlusion. However, there is leftward SR motion that abruptly ends at 2205 UTC after the low-ρ_{HV} band swept

[8] We also cannot rule out that changes in radial velocity may be influenced by tornado debris centrifuging rather than momentum surges.

Brought to you by NOAA Central Library | Unauthenticated | Downloaded 09/15/21 06:16 PM UTC

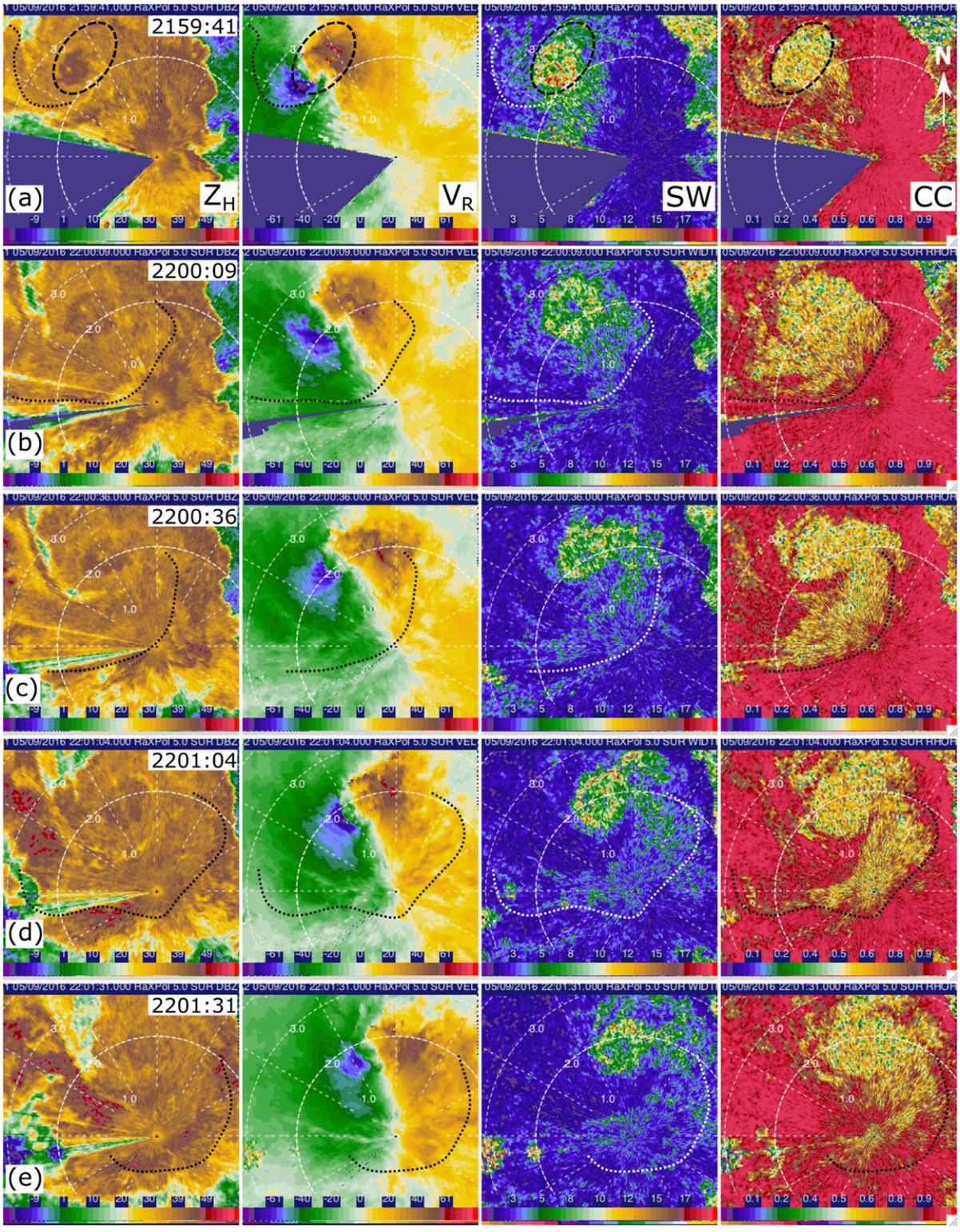

FIG. 14. RaXPol PPIs from (a) 2159:41, (b) 2200:09, (c) 2200:36, (d) 2201:04, and (e) 2201:31 UTC at 5.0° elevation of (left) radar reflectivity (dBZ), (second column) radial velocity (m s^{-1}), (third column) spectrum width (m s^{-1}), and (right) copolar correlation coefficient. Annotated as a black dotted oval in (a) is the area of the TDS and in (a)–(e) dotted lines are the approximate forward edge of the reduced area of copolar correlation coefficient associated with a likely debris ejection from a RFD internal momentum surge. Range rings are every 1 km. All of the PPIs are centered in the same location. The approximate center beam height at the location of the TDS ranges from ~150 to 200 m ARL.

Brought to you by NOAA Central Library | Unauthenticated | Downloaded 09/15/21 06:16 PM UTC

through the hook echo. In addition, the band was already present when data collection began, so we cannot rule out that such a failed occlusion had already occurred.

The origin of the implied internal RFD momentum surge cannot be determined from the available data. One possibility is that an influx of a large concentration of larger raindrops (e.g., Fig. 11) contributed to RFD enhancement, which also would indicate the preferential evaporation of small drops and attendant increase in negative buoyancy. Surges have been hypothesized to contribute to tornadogenesis (e.g., Kosiba et al. 2013; Marquis et al. 2016), and, in some cases discussed in Marquis et al. (2012), to tornado maintenance, both via baroclinic generation of near-surface horizontal vorticity and increased convergence along the boundary [e.g., see Figs. 15c and 16 in Marquis et al. (2012)]. However, they also may contribute to tornado dissipation if they are associated with excessive negative buoyancy and/or near-surface divergence. Most relevant to such a possibility for this case are the observations of Lee et al. (2012), who documented several internal RFD momentum surges in the Bowdle, SD, tornadic supercell. However, only the final one was accompanied by large near-surface negative buoyancy in the vicinity of the tornado, which occurred simultaneously with increased misalignment between the tornado and the storm updraft (as approximated from a weak-echo hole) as the tornado dissipated. Similarly, Schenkman et al. (2016) identified both ''warm'' and ''cold'' internal RFD momentum surges within the same simulated supercell at different times. However, there are plausible alternative possibilities for their origin in this case as well. The positioning of the ostensible surge is consistent with generation from perturbations in horizontal pressure gradient forces (PGFs) within the RFD; in such a scenario, the enhanced downdraft region is driven primarily by downward-directed PGFs (Skinner et al. 2015).

Nonetheless, we lack the data to definitively prove a connection between an internal RFD momentum surge and tornado dissipation in this case. Ideally, future studies using rapid-scan dual-Doppler analysis combined with near-surface thermodynamic data are needed to better elucidate how internal RFD momentum surges affect existing tornadoes (e.g., Marquis et al. 2016).

Finally, a number of studies have now identified TVS characteristics that are associated with tornado dissipation. However, the prospect that some of these behaviors might undergo regular oscillations owing to internal storm processes that only sometimes contribute to tornado dissipation is troubling for their possible use in operational nowcasting. More rapid-scan case studies are needed to better identify not only TVS characteristics leading up to dissipation, but to determine how consistently in time such behaviors must occur before there is increased confidence that imminent dissipation is likely. Mobile Doppler radar case studies, ideally using dual-Doppler analyses, also can better identify features that cause observed TVS behaviors. In addition, there have now been several cases in which dissipation was preceded by increases in median hook echo Z_{DR}, and in this study there is also an increase in median hook echo K_{DP}, perhaps consistent with hypothesized increases in negatively buoyant surface air that disrupts tornado maintenance. These results combined with circumstantial evidence provided in Van Den Broeke (2017) of changes in polarimetric signatures between tornado formation and dissipation motivates a study of a large number of tornadic supercells to investigate polarimetric features and signatures that may occur prior to tornado dissipation. Subsequent efforts may elucidate more clearly how TVS and storm-scale polarimetric features together may be leveraged, if at all, into tornado life cycle nowcasting in the future.

Acknowledgments. The authors thank Jeff Snyder (NSSL) for his help with the DSD retrieval algorithm. Comments from Patrick Skinner (OU/CIMMS/NSSL), Jim Kurdzo (MIT), and one anonymous reviewer greatly enhanced the quality of this study. This study was funded by NSF Grant AGS-1748177 (French), AGS-1748191 (Kingfield), and AGS-1262048 and AGS-1560945 (Bluestein).

REFERENCES

Alexander, C. R., 2010: A mobile radar based climatology of supercell tornado structure and dynamics. Ph.D. dissertation, University of Oklahoma, 229 pp.

——, and J. Wurman, 2005: The 30 May 1998 Spencer, South Dakota, storm. Part I: The structural evolution and environment of the tornadoes. *Mon. Wea. Rev.*, **133**, 72–97, https://doi.org/10.1175/MWR-2855.1.

Beck, J. R., J. L. Schroeder, and J. M. Wurman, 2006: High-resolution dual-Doppler analyses of the 29 May 2001 Kress, Texas, cyclic supercell. *Mon. Wea. Rev.*, **134**, 3125–3148, https://doi.org/10.1175/MWR3246.1.

Bluestein, H. B., and A. L. Pazmany, 2000: Observations of tornadoes and other convective phenomena with a mobile, 3-mm wavelength, Doppler radar: The spring 1999 field experiment. *Bull. Amer. Meteor. Soc.*, **81**, 2939–2951, https://doi.org/10.1175/1520-0477(2000)081<2939:OOTAOC>2.3.CO;2.

——, ——, J. C. Galloway, and R. E. McIntosh, 1995: Studies of the substructure of severe convective storms using a mobile 3-mm-wavelength Doppler radar. *Bull. Amer. Meteor. Soc.*, **76**, 2155–2169, https://doi.org/10.1175/1520-0477(1995)076<2155:SOTSOS>2.0.CO;2.

——, C. C. Weiss, and A. L. Pazmany, 2003: Mobile Doppler radar observations of a tornado in a supercell near Bassett, Nebraska, on 5 June 1999. Part I: Tornadogenesis. *Mon. Wea. Rev.*, **131**, 2954–2967, https://doi.org/10.1175/1520-0493(2003)131<2954:MDROOA>2.0.CO;2.

Brought to you by NOAA Central Library | Unauthenticated | Downloaded 09/15/21 06:16 PM UTC

——, M. M. French, R. L. Tanamachi, S. Frasier, K. Hardwick, F. Junyent, and A. Pazmany, 2007: Close-range observations of tornadoes in supercells made with a dual-polarization, X-band, mobile Doppler radar. *Mon. Wea. Rev.*, **135**, 1522–1543, https://doi.org/10.1175/MWR3349.1.

——, ——, I. PopStefanija, R. T. Bluth, and J. B. Knorr, 2010: A mobile, phased-array Doppler radar for the study of severe convective storms. *Bull. Amer. Meteor. Soc.*, **91**, 579–600, https://doi.org/10.1175/2009BAMS2914.1.

——, K. J. Thiem, J. C. Snyder, and J. B. Houser, 2018: The multiple-vortex structure of the El Reno, Oklahoma, tornado on 31 May 2013. *Mon. Wea. Rev.*, **146**, 2483–2502, https://doi.org/10.1175/MWR-D-18-0073.1.

——, ——, ——, and ——, 2019: Tornadogenesis and early tornado evolution in the El Reno, Oklahoma, supercell on 31 May 2013. *Mon. Wea. Rev.*, **147**, 2045–2066, https://doi.org/10.1175/MWR-D-18-0338.1.

Bodine, D. J., M. R. Kumjian, R. D. Palmer, P. L. Heinselman, and A. V. Ryzhkov, 2013: Tornado damage estimation using polarimetric radar. *Wea. Forecasting*, **28**, 139–158, https://doi.org/10.1175/WAF-D-11-00158.1.

Burgess, D. W., V. T. Wood, and R. A. Brown, 1982: Mesocyclone evolution statistics. Preprints, *12th Conf. on Severe Local Storms*, San Antonio, TX, Amer. Meteor. Soc., 422–424.

Byko, Z., P. Markowski, Y. Richardson, J. Wurman, and E. Adlerman, 2009: Descending reflectivity cores in supercell thunderstorms observed by mobile radars and in a high-resolution numerical simulation. *Wea. Forecasting*, **24**, 155–186, https://doi.org/10.1175/2008WAF2222116.1.

Calhoun, K. M., D. R. MacGorman, C. L. Ziegler, and M. I. Biggerstaff, 2013: Evolution of lightning activity and storm charge relative to dual-Doppler analysis of a high-precipitation supercell storm. *Mon. Wea. Rev.*, **141**, 2199–2223, https://doi.org/10.1175/MWR-D-12-00258.1.

Cao, Q., G. Zhang, E. Brandes, T. Schuur, A. Ryzhkov, and K. Ikeda, 2008: Analysis of video disdrometer and polarimetric radar data to characterize rain microphysics in Oklahoma. *J. Appl. Meteor. Climatol.*, **47**, 2238–2255, https://doi.org/10.1175/2008JAMC1732.1.

Chrisman, J. N., 2013: Dynamic scanning. *NEXRAD Now*, No. 22, WSR-88D Radar Operations Center, Norman, OK, 1–3, https://www.roc.noaa.gov/WSR88D/PublicDocs/NNOW/NNow22c.pdf.

——, 2014: Multiple Elevation Scan Option for SAILS (MESO-SAILS)—The next step in dynamic scanning for the WSR-88D. WSR-88D Radar Operations Center, 27 pp.

Darkow, G. L., and J. C. Roos, 1970: Multiple tornado producing thunderstorms and their apparent cyclic variations in intensity. Preprints, *14th Conf. on Radar Meteorology*, Tucson, AZ, Amer. Meteor. Soc., 305–308.

Dowell, D. C., and H. B. Bluestein, 2002a: The 8 June 1995 McLean, Texas, storm. Part I: Observations of cyclic tornadogenesis. *Mon. Wea. Rev.*, **130**, 2626–2648, https://doi.org/10.1175/1520-0493(2002)130<2626:TJMTSP>2.0.CO;2.

——, and ——, 2002b: The 8 June 1995 McLean, Texas, storm. Part II: Cyclic tornado formation, maintenance, and dissipation. *Mon. Wea. Rev.*, **130**, 2649–2670, https://doi.org/10.1175/1520-0493(2002)130<2649:TJMTSP>2.0.CO;2.

French, M. M., and D. M. Kingfield, 2019: Dissipation characteristics of tornadic vortex signatures associated with long-duration tornadoes. *J. Appl. Meteor. Climatol.*, **58**, 317–339, https://doi.org/10.1175/JAMC-D-18-0187.1.

——, H. B. Bluestein, D. C. Dowell, L. J. Wicker, M. R. Kramar, and A. L. Pazmany, 2008: High-resolution, mobile Doppler radar observations of cyclic mesocyclogenesis in a supercell. *Mon. Wea. Rev.*, **136**, 4997–5016, https://doi.org/10.1175/2008MWR2407.1.

——, ——, I. PopStefanija, C. A. Baldi, and R. T. Bluth, 2013: Reexamining the vertical development of tornadic vortex signature in supercells. *Mon. Wea. Rev.*, **141**, 4576–4601, https://doi.org/10.1175/MWR-D-12-00315.1.

——, ——, ——, ——, and ——, 2014: Mobile, phased-array, Doppler radar observations of tornadoes at X band. *Mon. Wea. Rev.*, **142**, 1010–1036, https://doi.org/10.1175/MWR-D-13-00101.1.

——, D. W. Burgess, E. R. Mansell, and L. J. Wicker, 2015a: Bulk hook echo raindrop sizes retrieved using mobile, polarimetric Doppler radar observations. *J. Appl. Meteor. Climatol.*, **54**, 423–450, https://doi.org/10.1175/JAMC-D-14-0171.1.

——, P. S. Skinner, L. J. Wicker, and H. B. Bluestein, 2015b: Documenting a rare tornado merger observed in the 24 May 2011 El Reno–Piedmont, Oklahoma, supercell. *Mon. Wea. Rev.*, **143**, 3025–3043, https://doi.org/10.1175/MWR-D-14-00349.1.

Griffin, C. B., C. C. Weiss, A. E. Reinhart, J. C. Snyder, H. B. Bluestein, J. Wurman, and K. A. Kosiba, 2018: In situ and radar observations of the low reflectivity ribbon in supercells during VORTEX2. *Mon. Wea. Rev.*, **146**, 307–327, https://doi.org/10.1175/MWR-D-17-0201.1.

——, D. J. Bodine, J. M. Kurdzo, A. Mahre, and R. D. Palmer, 2019: High-temporal resolution observations of the 27 May 2015 Canadian, Texas, tornado using the atmospheric imaging radar. *Mon. Wea. Rev.*, **147**, 873–891, https://doi.org/10.1175/MWR-D-18-0297.1.

——, ——, and R. Palmer, 2020: Polarimetric radar observations of simultaneous tornadoes on 10 May 2010 near Norman, Oklahoma. *Mon. Wea. Rev.*, **148**, 477–497, https://doi.org/10.1175/MWR-D-19-0156.1.

Houser, J. L., H. B. Bluestein, and J. C. Snyder, 2015: Rapid-scan, polarimetric, Doppler radar observations of tornadogenesis and tornado dissipation in a tornadic supercell: The El Reno, Oklahoma storm of 24 May 2011. *Mon. Wea. Rev.*, **143**, 2685–2710, https://doi.org/10.1175/MWR-D-14-00253.1.

——, ——, and J. Snyder, 2016: A finescale radar examination of the tornadic debris signature and weak-echo reflectivity band associated with a large, violent tornado. *Mon. Wea. Rev.*, **144**, 4101–4130, https://doi.org/10.1175/MWR-D-15-0408.1.

Isom, B., and Coauthors, 2013: The Atmospheric Imaging Rader: Simultaneous volumetric observations using a phased array weather radar. *J. Atmos. Oceanic Technol.*, **30**, 655–675, https://doi.org/10.1175/JTECH-D-12-00063.1.

Kosiba, K., J. M. Wurman, Y. P. Richardson, P. M. Markowski, P. Robinson, and J. Marquis, 2013: Genesis of the Goshen County, Wyoming, tornado on 5 June 2009 during VORTEX2. *Mon. Wea. Rev.*, **141**, 1157–1181, https://doi.org/10.1175/MWR-D-12-00056.1.

Kumjian, M. R., and A. V. Ryzhkov, 2008: Polarimetric signatures in supercell thunderstorms. *J. Appl. Meteor. Climatol.*, **47**, 1940–1961, https://doi.org/10.1175/2007JAMC1874.1.

——, A. P. Khain, N. Benmoshe, E. Ilotoviz, A. V. Ryzhkov, and V. T. J. Phillips, 2014: The anatomy and physics of Z_{DR} columns: Investigating a polarimetric radar signature with a spectral bin microphysical model. *J. Appl. Meteor. Climatol.*, **53**, 1820–1843, https://doi.org/10.1175/JAMC-D-13-0354.1.

Kurdzo, J. M., D. J. Bodine, B. L. Cheong, and R. D. Palmer, 2015: High-temporal resolution polarimetric X-band Doppler radar observations of the 20 May 2013 Moore, Oklahoma, tornado.

Brought to you by NOAA Central Library | Unauthenticated | Downloaded 09/15/21 06:16 PM UTC

Mon. Wea. Rev., **143**, 2711–2735, https://doi.org/10.1175/MWR-D-14-00357.1.

——, and Coauthors, 2017: Observations of severe local storms and tornadoes with the Atmospheric Imaging Radar. *Bull. Amer. Meteor. Soc.*, **98**, 915–935, https://doi.org/10.1175/BAMS-D-15-00266.1.

Lee, B. D., C. A. Finley, and C. D. Karstens, 2012: The Bowdle, South Dakota, cyclic tornadic supercell of 22 May 2010: Surface analysis of rear-flank downdraft evolution and multiple internal surges. *Mon. Wea. Rev.*, **140**, 3419–3441, https://doi.org/10.1175/MWR-D-11-00351.1.

Mahre, A., J. M. Kurdzo, D. J. Bodine, C. B. Griffin, R. D. Palmer, and T. Yu, 2018: Analysis of the 16 May 2015 Tipton, Oklahoma, EF-3 tornado at high spatiotemporal resolution using the Atmospheric Imaging Radar. *Mon. Wea. Rev.*, **146**, 2103–2124, https://doi.org/10.1175/MWR-D-17-0256.1.

Marquis, J. N., Y. P. Richardson, P. Markowski, D. Dowell, and J. Wurman, 2012: Tornado maintenance investigated with high-resolution dual-Doppler and EnKF analysis. *Mon. Wea. Rev.*, **140**, 3–27, https://doi.org/10.1175/MWR-D-11-00025.1.

——, ——, ——, J. Wurman, K. Kosiba, and P. Robinson, 2016: An investigation of the Goshen County, Wyoming, tornadic supercell of 5 June 2009 using EnKF assimilation of mobile mesonet and radar observations collected during VORTEX2. Part II: Mesocyclone-scale processes affecting tornado formation, maintenance, and decay. *Mon. Wea. Rev.*, **144**, 3441–3463, https://doi.org/10.1175/MWR-D-15-0411.1.

Oye, R., C. Mueller, and S. Smith, 1995: Software for radar translation, visualization, editing, and interpolation. Preprints, *29th Conf. on Radar Meteorology*, Vail, CO, Amer. Meteor. Soc., 359–361.

Pazmany, A. L., J. B. Mead, H. B. Bluestein, J. C. Snyder, and J. B. Houser, 2013: A mobile, rapid-scanning, X-band, polarimetric (RaXPol) Doppler radar system. *J. Atmos. Oceanic Technol.*, **30**, 1398–1413, https://doi.org/10.1175/JTECH-D-12-00166.1.

Richardson, L. M., W. D. Zittel, R. R. Lee, V. M. Melnikov, R. L. Ice, and J. G. Cunningham, 2017: Bragg scatter detection by the WSR-88D. Part II: Assessment of ZDR bias estimation. *J. Atmos. Oceanic Technol.*, **34**, 479–493, https://doi.org/10.1175/JTECH-D-16-0031.1.

Ryzhkov, A., T. J. Schuur, D. W. Burgess, and D. S. Zrnić, 2005: Polarimetric tornado detection. *J. Appl. Meteor.*, **44**, 557–570, https://doi.org/10.1175/JAM2235.1.

Schenkman, A. D., M. Xue, and D. T. Dawson, 2016: The cause of internal outflow surges in a high-resolution simulation of the 8 May 2003 Oklahoma City tornadic supercell. *J. Atmos. Sci.*, **73**, 353–370, https://doi.org/10.1175/JAS-D-15-0112.1.

Skinner, P. S., C. C. Weiss, L. J. Wicker, C. K. Potvin, and D. C. Dowell, 2015: Forcing mechanisms for an internal rear-flank downdraft momentum surge in the 18 May 2010 Dumas, Texas, supercell. *Mon. Wea. Rev.*, **143**, 4305–4330, https://doi.org/10.1175/MWR-D-15-0164.1.

Snyder, J. C., and H. B. Bluestein, 2014: Some considerations for the use of high-resolution mobile radar data in tornado intensity determination. *Wea. Forecasting*, **29**, 799–827, https://doi.org/10.1175/WAF-D-14-00026.1.

——, ——, V. Venkatesh, and S. J. Frasier, 2013: Observations of polarimetric signatures in supercells by an X-band mobile Doppler radar. *Mon. Wea. Rev.*, **141**, 3–29, https://doi.org/10.1175/MWR-D-12-00068.1.

Spoden, P. J., R. A. Wolf, and L. R. Lemon, 2012: Operational uses of spectrum width. *Electron. J. Severe Storms Meteor.*, **7** (2), https://ejssm.org/ojs/index.php/ejssm/article/view/86.

Van Den Broeke, M. S., 2017: Polarimetric radar metrics related to tornado life cycles and intensity in supercell storms. *Mon. Wea. Rev.*, **145**, 3671–3686, https://doi.org/10.1175/MWR-D-16-0453.1.

Wakimoto, R. M., N. T. Atkins, K. M. Butler, H. B. Bluestein, K. Thiem, J. Snyder, and J. Houser, 2015: Photogrammetric analysis of the 2013 El Reno tornado combined with mobile X-band polarimetric radar data. *Mon. Wea. Rev.*, **143**, 2657–2683, https://doi.org/10.1175/MWR-D-15-0034.1.

——, and Coauthors, 2016: Aerial damage survey of the 2013 El Reno tornado combined with mobile radar data. *Mon. Wea. Rev.*, **144**, 1749–1776, https://doi.org/10.1175/MWR-D-15-0367.1.

——, Z. Wienhoff, H. B. Bluestein, and D. Reif, 2018: The Dodge City tornadoes on 24 May 2016: Damage survey, photogrammetric analysis combined with mobile polarimetric radar data. *Mon. Wea. Rev.*, **146**, 3735–3771, https://doi.org/10.1175/MWR-D-18-0125.1.

——, ——, ——, D. J. Bodine, and J. M. Kurdzo, 2020: Mobile radar observations of the evolving debris field compared with a damage survey of the Shawnee, Oklahoma, tornado of 19 May 2013. *Mon. Wea. Rev.*, **148**, 1779–1803, https://doi.org/10.1175/MWR-D-19-0215.1.

Wienhoff, Z. B., H. B. Bluestein, L. J. Wicker, J. C. Snyder, A. Shapiro, C. K. Potvin, J. B. Houser, and D. W. Reif, 2018: Applications of a spatially variable advection correction technique for temporal correction of dual-Doppler analyses of tornadic supercells. *Mon. Wea. Rev.*, **146**, 2949–2971, https://doi.org/10.1175/MWR-D-17-0360.1.

Wood, V. T., and R. A. Brown, 1997: Effects of radar sampling on single-Doppler velocity signatures of mesocyclones and tornadoes. *Wea. Forecasting*, **12**, 928–938, https://doi.org/10.1175/1520-0434(1997)012<0928:EORSOS>2.0.CO;2.

Wurman, J., 2002: The multiple-vortex structure of a tornado. *Wea. Forecasting*, **17**, 473–505, https://doi.org/10.1175/1520-0434(2002)017<0473:TMVSOA>2.0.CO;2.

——, and S. Gill, 2000: Finescale radar observations of the Dimmitt, Texas (2 June 1995), tornado. *Mon. Wea. Rev.*, **128**, 2135–2164, https://doi.org/10.1175/1520-0493(2000)128<2135:FROOTD>2.0.CO;2.

——, and K. Kosiba, 2013: Finescale radar observations of tornado and mesocyclone structures. *Wea. Forecasting*, **28**, 1157–1174, https://doi.org/10.1175/WAF-D-12-00127.1.

——, J. Straka, E. Rasmussen, M. Randall, and A. Zahrai, 1997: Design and deployment of a portable, pencil-beam, pulsed, 3-cm Doppler radar. *J. Atmos. Oceanic Technol.*, **14**, 1502–1512, https://doi.org/10.1175/1520-0426(1997)014<1502:DADOAP>2.0.CO;2.

——, D. Dowell, Y. Richardson, P. Markowski, E. Rasmussen, D. Burgess, L. Wicker, and H. B. Bluestein, 2012: The second Verification of the Origins of Rotation in Tornadoes Experiment: VORTEX2. *Bull. Amer. Meteor. Soc.*, **93**, 1147–1170, https://doi.org/10.1175/BAMS-D-11-00010.1.

——, K. Kosiba, P. Robinson, and T. Marshall, 2014: The role of multiple-vortex tornado structure in causing storm researcher fatalities. *Bull. Amer. Meteor. Soc.*, **95**, 31–45, https://doi.org/10.1175/BAMS-D-13-00221.1.

Zrnić, D. S., G. Zhang, and R. J. Doviak, 2011: Bias correction and Doppler measurement for polarimetric phased-array radar. *IEEE Trans. Geosci. Remote Sens.*, **49**, 843–853, https://doi.org/10.1109/TGRS.2010.2057436.

Brought to you by NOAA Central Library | Unauthenticated | Downloaded 09/15/21 06:16 PM UTC